ACS Catalysis

pubs.acs.org/acscatalysis
Research Article

Molecular-Level Mechanistic Insights into PETase-Catalyzed Plastics Hydrolysis from Accurate QM/MM Free Energy Calculations

Alessandro Berselli,* Maria Cristina Menziani, GiovanniMaria Piccini,* and Francesco Muniz-Miranda

Cite This: *ACS Catal.* 2025, 15, 10702−10721
Read Online

ACCESS | Metrics & More | Article Recommendations | Supporting Information

ABSTRACT: The enzyme PETase is capable of depolymerizing plastics such as polyethylene terephthalate (PET) at moderate temperatures, and demonstrated even higher activity toward polyethylene-2,5-furan dicarboxylate (PEF), opening promising routes for the efficient upcycling of plastic wastes. To fully exploit the potential of these biocatalytic systems, an understanding of the mechanism of their activity at the atomistic level is pivotal. To this end, this study investigates two fundamental stages of the catalytic cycle of PET and PEF hydrolysis by PETase—acylation and deacylation—using hybrid QM/MM enhanced sampling molecular dynamics simulations to capture all relevant dynamic effects. Well-tempered metadynamics simulations at the DFTB3 level are performed along collective variables optimized via linear discriminant analysis, a supervised learning-assisted approach that accounts for the contributions of each potentially relevant degree of freedom. The free energy (FE) profiles indicate that the acylation stage is the rate-limiting step for both PET and PEF degradation, with barriers ≈ 8 kcal/mol and ≈ 4 kcal/mol higher than those obtained for the deacylation step, respectively. Remarkably, substantial mechanistic differences are found. While PET acylation occurs in a concerted manner, with a single energy barrier of ≈ 21 kcal/mol, PEF acylation follows a two-step mechanism where after the first barrier, ≈ 10 kcal/mol high, a metastable intermediate state is formed, which then evolves toward the product once a second barrier of ≈ 2 kcal/mol is overcome. This mechanistic description is consistent with the FE profiles obtained at higher levels of theory (PBE, B3LYP, RI-MP2) via FE perturbation, thus validating the key insights elucidated by metadynamics simulations. Finally, both global and local reactivity descriptors derived from conceptual density functional theory suggest that PEF is more electrophilic and susceptible to nucleophilic attack than PET. The results obtained by means of the robust computational protocol adopted here offer thermodynamic and mechanistic insights into PET and PEF hydrolysis by PETase at the molecular level, corroborating the experimentally observed enhanced activity of this enzyme toward PEF. The distinctive hallmarks of PETase depolymerization uncovered in this work provide valuable foundations for enzyme engineering efforts aimed at developing *universal* biocatalysts for semiaromatic plastic recycling, ultimately paving the way for efficient application in industrial settings.

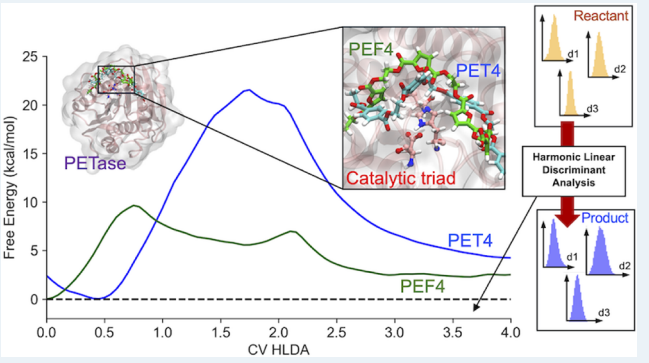

KEYWORDS: *PETase, polyethylene terephthalate, polyethylene −2, 5- furan dicarboxylate, linear discriminant analysis, QM/MM molecular dynamics simulations, well-tempered metadynamics*

INTRODUCTION

The extensive diffusion of plastic materials over the last decades has become a critical environmental challenge, threatening ecosystems worldwide. From the accumulation of plastic debris in soils to the pervasive spread of micro- and nanoplastics in marine environments, the adverse effects of plastic pollution are well-documented.[1−3] Among these polymers, polyethylene terephthalate (PET) stands out due to its widespread use, driven by its distinctive properties. Durability, gas and water barrier properties, transparency, and low cost make this material ideal for manufacturing single-use food and beverage containers.[4] However, the fate of these manufacts after their use is still far from being environmentally sustainable.[5] Moreover, the synthesis of these polymers is sourced by fossil raw materials, whose availability is limited and the value chain is highly energy demanding.[6] Finally, PET recycling is still not an attractive solution because processed materials lose most their properties and the treatment is economically disadvantageous compared to the production from fossil fuel monomers.[7]

Received: February 18, 2025
Revised: May 28, 2025
Accepted: May 28, 2025

To address these challenges, biobased packaging materials have emerged as a promising alternative to reduce the carbon footprint and to lower environmental impact than petroleum-based plastics.[6] A remarkable example is the sugar-derived polyethylene-2,5-furan dicarboxylate (PEF), which combines reduced greenhouse gas emissions during synthesis with nontoxicity and comparable mechanical properties to PET, positioning it as a valuable potential substitute in the near future.[8]

In this scenario, finding efficient solutions for the sustainable and efficient upcycling of plastic debris is mandatory. In the last years, an environmentally friendly and sustainable alternative to conventional methods has been offered by enzymatic degradation.[9] Several bacterial enzymes were discovered able to cleave the polymeric plastic chains, including cutinases, lipases, and esterases, and grouped in the family of "PET-hydrolyzing enzymes" (PHEs).[10,11] A breakthrough in this field occurred in 2016 with the discovery of a bacterium, named *Ideonella Sakaiensis 201-F6* that used PET as a major nutrient thanks to the secretion of two hydrolases: PETase and MHETase.[12] Working synergistically, PETase cleaves the PET chains mainly into *mono*(hydroxyethyl terephthalate) (MHET), *bis*(hydroxyethyl terephthalate) (BHET), terephthalic acid (TPA), and ethylene glycol (EG; Figure 1A), whereas MHETase completes the process, converting MHET and BHET into their minimal chemical moieties. Remarkably, PETase has also demonstrated significant hydrolytic activity against PEF,[13] depolymerizing this semiaromatic polyester into *mono*(2-hydroxyethyl furanoate) (MHEF), *bis*(2-hydroxyethyl furanoate) (BHEF) and 2−5 furandicarboxylic acid (FDCA) and ethylene glycol (EG; Figure 1B).[14]

From a structural point of view, PETase resembles the folding of an α/β hydrolase, characterized by a central nine-stranded twisted β-strand, surrounded by seven α-helices.[13,15−17] The catalysis is exerted by a catalytic triad composed of serine, histidine, and aspartate residues (S160, H237, and D206) in the active site, which encompasses also the residues tryptophane, tyrosine, methionine and isoleucine (W185, Y87, M161, and I208) to support the substrate recognition and binding[15] (Figure 1C). The key peculiarity of PETase is that it achieves peak activity at relatively low temperature (≈ 30 °C) thanks to the flexibility of the binding pocket, which facilitates the accommodation of the polymeric chains. In contrast, its catalytic efficiency drops at a higher temperature because of its poor thermostability.[15]

While these characteristics facilitate new pathways for managing plastic waste under moderate conditions, they may also limit these systems' applicability for degrading high-crystallinity PET waste, which requires operating near the material's glass transition temperature (≈ 79 °C).[18,19] For this reason, the recent years have witnessed the introduction of a number of variants of PETase, which were strategically modified to improve its structural stability and catalytic activity.[16,20−26]

In a recent work of some of us,[27] the structural properties and binding of PETase with tetrameric chains of PET (PET4, Figure 1D) and PEF (PEF4, Figure 1E) were investigated through an extensive application of molecular modeling techniques. Specifically, molecular docking, molecular dynamics (MD) simulations and unbinding free energy (FE) calculations indicated that PET4 is stabilized within the binding pocket of the enzymes thanks to the aromatic

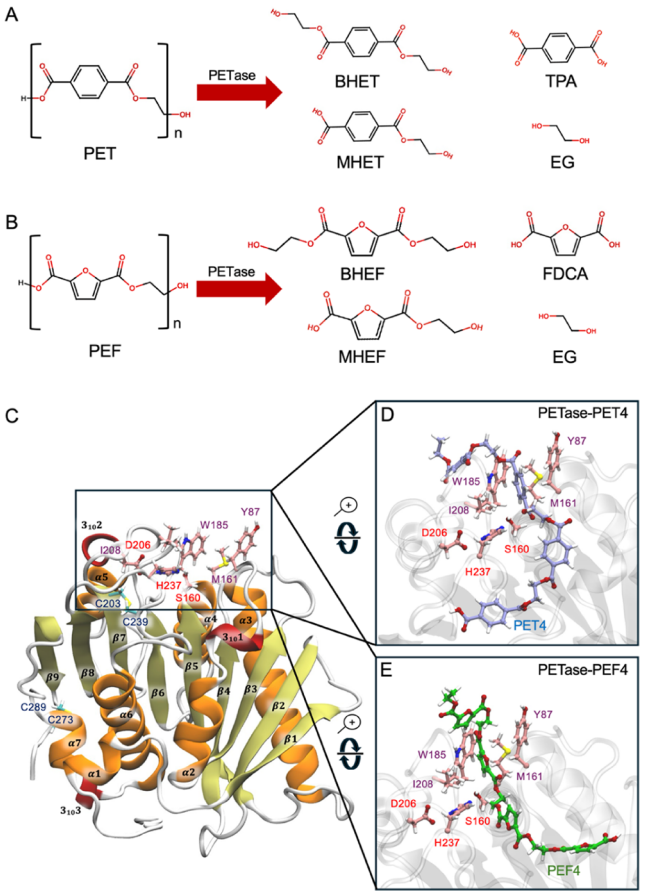

Figure 1. Structure and enzymatic biodegradation of PET and PEF by PETase. Main (monomeric) products of depolymerization of PET and PEF by PETase: (**A**) BHET, MHET, TPA and EG for PET and (**B**) BHEF, MHEF, FDCA and EG for PEF. (**C**) Structure of PETase (PDB ID: 5XJH[16]). The protein is colored according to its secondary structure elements: yellow for the nine β-strands, orange for the seven α-helices, red for the three 3_{10}-helices and gray for unfolded regions. Distinctive amino acids are also shown in sticks: cysteines C273 - C289 and C203 − C239 forming two disulfide bridges are colored in cyan, the residues S160, H237, D206 (catalytic triad), W185, I208, M161 and Y87 forming the active site are colored in pink. Close-up views of the catalytic site with the (**D**) PET4 and (**E**) PEF4 bound chains, represented as ice blue and green sticks, respectively, are shown.

interactions established by the TPA moieties of PET4 with the W185 and Y87 side chains. Conversely, PEF4 formed weak interactions with the enzymes, quickly dissociating from the PETase binding pocket during MD simulations. However, that preliminary assessment did not examine the reaction mechanisms of the enzyme with these substrates.

The hydrolysis of PET by PETase has been undertaken by various studies[28−33] that used multiscale quantum mechanics/molecular mechanics (QM/MM) MD simulations to investigate the elementary steps of the catalytic cycle. The process is initiated by the nucleophilic attack of S160 to the hydrolyzable ester C atom of PET (acylation). This stage is activated by the abstraction of a proton from the S160 hydroxyl side chain by H237 and leads to the formation of an acyl-enzyme intermediate. Then, a water molecule enters the active site and attacks the acyl-enzyme intermediate, completing the hydrolysis of PET and restoring the enzyme to its initial state (deacylation). These steps proceed through the formation of

https://doi.org/10.1021/acscatal.5c01263
ACS Catal. 2025, 15, 10702−10721

Scheme 1. Representation of the PET Hydrolysis Mechanism by PETase[a]

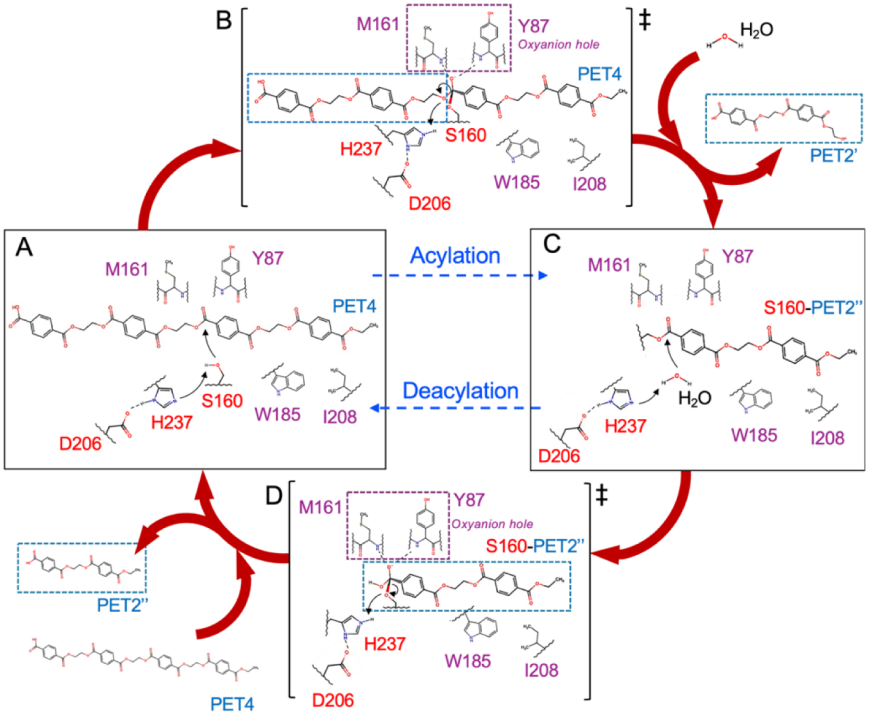

[a]The scheme is represented using the PET4 model as a substrate. In each panel, the amino acids in the active site are shown: the catalytic triad (S160, H237, D206) is indicated in red, whereas W185, Y87, M161 and I208 are in purple. (**A**) The reaction starts with the deprotonation of S160 by H237 and the nucleophilic attack of the PET4 ester group. (**B**) A negatively charged tetrahedral transition state is formed, stabilized by the oxyanion hole formed by Y87 and M161 backbones. (**C**) The TS decomposes and forms the acyl-enzyme intermediate (S160-PET2''), completing the acylation stage. The first product of the hydrolysis leaves the catalytic domain (PET2'), followed by the entry of a water molecule within the binding pocket, which triggers the deacylation. (**D**) The reaction proceeds with the formation of a second negatively charged TS, stabilized by the oxyanion hole. Then, the second product of depolymerization is formed (PET2''), the enzyme is restored to its initial state and ready to restart the cycle with the binding of a new chain of PET

tetrahedral transition states where the carbonyl O atom of the substrate is stabilized by the backbone of the M161 and Y87 (oxyanion hole) (Scheme 1).

While some insights from these studies point to common features of the reaction mechanism, other results remain debated. In particular, the two-steps[17,28,31,32] versus four-steps[29,33] nature of the process, as well as identification of the rate-limiting step, are still open questions, thus highlighting the necessity of further investigation to deeper understand the underlying hydrolysis mechanism at the molecular level. Furthermore, none of the studies published so far delved into the assessment of the reaction mechanism of PEF depolymerization.

Building on these findings, in this study we aim to address these gaps of knowledge by studying the catalysis of PET4 and PEF4 by PETase using QM/MM MD simulations.

A crucial step in the study of chemical reactions is the selection of the reaction coordinate, which is defined by collective variables (CVs) capturing the slowest motions of the system, i.e., those functions of the atomic coordinates describing the slow degrees of freedom associated with the activated process of interest. At first glance, a straightforward strategy to select the CVs may seem using chemical intuition for the system under study. For example, the transition can be followed along specific bonds that are broken or formed during the reaction. Although this approach may provide a set of CVs that are physically and chemically meaningful, it inherently assumes that the reaction mechanism is known *a priori*, overlooking any other degree of freedom that might undergo changes during the transition. In the context of PETase reaction mechanism, some prior works estimated the FE landscapes using forming or breaking bonds as CVs,[28,29,31] whereas others adopted more sophisticated strategies. García-Meseguer et al.[32] utilized an adaptive string method to define the minimum FE path connecting reactants to the product, while Burgin and collaborators[30] used transition path sampling[34] and inertial likelihood maximization[35] to provide optimal mechanistic description of the acylation and deacylation steps, and validated the resulting reaction coordinates via committor probability test.

In this work, we defined the reaction coordinate by using harmonic linear discriminant analysis (HLDA),[36,37] a supervised learning classification technique. Given a limited information about the two metastable states of interest in their local equilibrium states, namely reactants and products, HLDA allows designing an efficient one-dimensional CV in the form of a linear combination of a set of simple descriptors, such as bond distances or coordination numbers.

A well-tempered metadynamics (WTMD)[38] energy bias has been applied along these CVs to help the system to overcome the FE barriers and favor transitions from reactants to products. To gather exhaustive statistics at an affordable computational cost, the QM region has been treated with the third-order density functional tight binding (DFTB3) Hamiltonian.[39] This level of theory found successful application in many contexts,[40,41] but it does not guarantee the same

https://doi.org/10.1021/acscatal.5c01263
ACS Catal. 2025, 15, 10702−10721

accuracy as density functional theory (DFT) nor that of higher level techniques such as post-Hartree−Fock (HF) methods. Unfortunately, despite the increasing power of computational infrastructures, running long simulations with such high-level methods is still unaffordable, forcing one to find compromises among the accuracy, size of the QM region and time scale of the simulations.

A cheap yet efficient method to overcome this problem, consists in applying free energy perturbation (FEP)[42] in combination with metadynamics simulations. This approach, known as MetaFEP,[43] achieves the accuracy of the target level of theory requiring only a relatively small number of single-point calculations on the expensive high-level potential energy surface, reducing the computational cost but ensuring the sampling of the configurational space. This allows validation of the mechanistic hypothesis provided by the low-level method used for sampling, DFTB3 in this work, by comparing the FE profile with those obtained using MetaFEP with higher-level methods, DFT or MP2, and checking the consistency of the hypothesis.

Finally, an atomistic explanation of the different reactivity observed for the two substrates from an energetic point of view is provided by the reactivity descriptors defined in the framework of conceptual DFT.[44]

By providing the first molecular-level comparison of the reaction mechanism of PET and PEF hydrolysis, this study offers new insights to expand the applicability of this enzyme to a wider range of semiaromatic plastic materials of industrial interest.

COMPUTATIONAL METHODS

Assembly of the PETase−Substrate Complexes. The starting configurations of the PETase-PET4 and PETase-PEF4 complexes were chosen from the equilibrated structures produced in our previous work.[27] In that study, the initial structure of the enzyme was selected from the protein databank (PDB ID: 5XJH[16]), while the PET4 and PEF4 chains were generated using the CHARMM-GUI Polymer Builder tool.[45] The protonation state of charged amino acids was predicted with PropKa3[46,47] for reference physiological pH = 7, consistent with previous works.[28,29]

Briefly, in the models selected, the PETase-substrate complexes are mainly stabilized by the aromatic interactions established by the benzene or furan ring with W185 and Y87 side chains located to the catalytic site. These interactions are responsible of the positioning of the ester carbon atom of PET4 or PEF4 at less than 5 Å from the oxygen atom of S160, distance compatible with the initiation of the nucleophilic attack.[13] Moreover, in line with other computational[48] and experimental[49] investigations, the substrate monomers not directly bound to the catalytic site do not establish persistent interactions with the PETase surface.[27]

As a first step, the coordinate files produced with the NAMD software[50] were converted into AMBER-compatible files[51,52] in order to perform the MD simulations with the *sander* engine. This software was used because of the native implementations of the DFTB3 level of theory[39] as well as the straightforward interface with other programs, including ORCA,[53] enabling the application of different QM methods. Therefore, the ligands were parametrized (PET4 or PEF4) using the *antechamber* suite included in AmberTools.[52] The AM1-BCC charges and the *gaff* force field were used, writing out the missing parameters with the *parmchk* package. Then, the solvent and seven neutralizing Cl^- ions were added, and the topology file was built with *tleap*. The ff14SB parameters were adopted for the protein[54] and the TIP3P model[55] for water, with a buffer region of at least 14 Å from any atom of the protein or the substrate to the edges of the simulation box. During this step, the disulfide bonds between cysteines C203 and C239 and between C273 and C289 of PETase were preserved. The final systems were inscribed inside rectangular boxes with size (80 × 80 × 70) $Å^3$, counting approximately 43,000 atoms each.

Harmonic Linear Discriminant Analysis. Harmonic Linear Discriminant Analysis (HLDA) systematically constructs the CV for the process of interest as a linear combination of an arbitrary number of descriptors of the system.[36,37] This method uses as an input the equilibrium distributions of a set of descriptors at the end points of each transition, i.e., in this case, the reactants and products of the acylation and deacylation steps) and looks for the direction that maximizes the distance between the two states' distributions (or classes) by using a modified version of Fisher's linear discriminant analysis (LDA) with harmonic weighting.[36,37] The method is described in detail in Section S1.

The solution of the eigenvalues problem reported in eq S1 provides the coefficients of the linear combination of the starting descriptors (d1−11, c1−3 in Figure S1). This defines a CV along which the projections of the reactant and product distributions are well separated, enabling highly efficient and accurate sampling that better distinguishes the two states in the FE space. In principle, each degree of freedom of the system can be included in the definition of the reaction coordinate, so that no *a priori* knowledge on the process is required. Indeed, the coefficients provided by HLDA describe the relative weight of the descriptors, indicating the relevance of each feature in driving the system from the reactants to the products.

The optimization of the HLDA variables from the descriptor distributions was performed with the python script deposited on the PLUMED-NEST repository (www.plumed-nest.org), with plumID:19.042.[36] A detailed description of the workflow is reported in Section S1.

Descriptors for the Acylation and Deacylation Steps. In principle, each degree of freedom of the system could be included in the definition of the HLDA reaction coordinate as its contribution in separating the different metastable states will be given by the eigenvalue obtained solving the Fisher's discriminant problem (eq S1). Here, we selected 10 interatomic distances (Figure S1, d1-d10) between the residues of the catalytic triad and the substrate (PET4 or PEF4) to describe the acylation step. Changes in these distances are considered as the key descriptors of the process, as they include the bonds that is broken (d1 and d3) and formed (d2, d6) during acylation, and the proton shuttle mediated by H237 (d4). The remaining distances capture potential topological rearrangements of the carbonyl moiety of the substrate (d5), of the relative orientation between the catalytic triad and the substrate (d7), and the inter-residue distances within the catalytic triad (d8-d10).

In the case of deacylation, an additional distance (d11) was included to account for the formation of the bond between the C_S atom of the substrate and the oxygen atom of the incoming water molecule, which occurs during the hydrolysis of the acyl−enzyme intermediate. Additionally, we monitored three coordination numbers (c1, c2, c3) describing the interactions of the water molecule within the active site. We considered the coordination numbers between the O atom of the water

https://doi.org/10.1021/acscatal.5c01263
ACS Catal. 2025, 15, 10702−10721

molecule (c1), the Nε atom of H237 (c2) or the hydroxyl Oγ atom of S160 (c3) with the two H atoms of water to account for the cleavage or formation of covalent bonds independent of which of the two H atoms is involved. Moreover, since the deacylation reaction involves comparing descriptors with different physical meanings (distances and coordination numbers), the descriptor values were preprocessed by subtracting the mean of each descriptor's data set, considering both distributions simultaneously, and normalizing the final data to a range of −1 to +1 before applying HLDA. The selected descriptors are defined in Table S1 along with the coefficients obtained via HLDA, whereas the atoms involved are illustrated in Figure 2. A representation of the distances

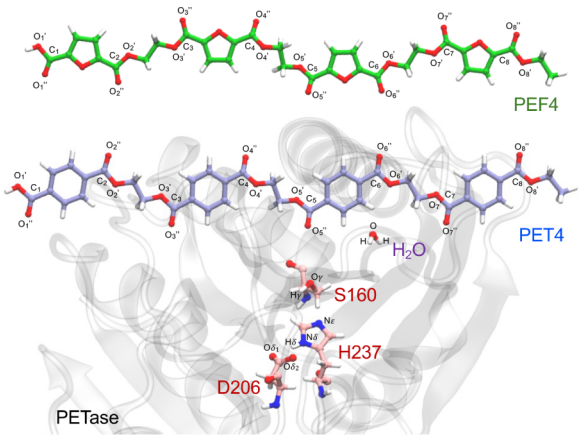

Figure 2. Atoms included in the descriptors used for HLDA. The labeled atoms correspond to those involved in the distances and coordination numbers defined in Table S1, which were used to construct the reaction coordinate via HLDA. PETase is depicted as a transparent gray cartoon, with the catalytic triad (S160, H237, and D206) highlighted. The two tetramers, PET4 and PEF4, are shown in a linear configuration for clarity.

and coordination numbers included in the analysis is provided in Figures S1A and S1B for the PETase-PET4 and PETase-PEF4 systems, respectively. The distributions of the descriptors collected from unbiased QM/MM MD simulations are shown in Figure S2.

QM/MM MD Simulations. As described before, HLDA requires as an input the equilibrium distributions of the selected features of each stable end point of the transition. These are collected from unbiased QM/MM MD simulations of reactant and products of both acylation and deacylation steps. For the acylation, we considered as reactant the system including enzyme and the substrate (PET4 or PEF4) and as a product the acyl-enzyme intermediate and the first leaving product (PET2' or PEF2'). For the deacylation, the acyl-enzyme intermediate was the reactant, and the product was the enzyme with the hydrolyzed substrate (PET2' + PET2'' or PEF2' + PEF2'').

The QM region was composed of the S160, H237, D206 side chains and the substrate (PET4 or PEF4), counting a total of 115 and 100 atoms for the PETase-PET4 and PETase-PEF4 complexes, respectively, and a net charge of −1. Moreover, one water molecule was included for the simulation of the end point states of the deacylation step to react with the acyl-enzyme intermediate in the active site. The configuration of the reactant state for the deacylation process was selected from the metadynamics QM/MM MD simulations performed to investigate the acylation stage. From the trajectory, we extracted one snapshot in which the system was in the acyl-enzyme intermediate state and (at least) one water molecule was found close to the catalytic triad. We labeled the water molecule, that was added to the QM region, and the system was used as a starting point for the QM/MM MD simulations performed to study the deacylation stage.

Each MD simulation was carried out with AMBER22,[51,52] treating the QM region at the DFTB3 level of theory,[39] using the default SCF convergence criteria of 10^{-8} kcal/mol. Concerning the MM domain of the system, we used the ff14SB[54] parameters for the protein along with the TIP3P model[55] for water. The particle mesh Ewald (PME) method was employed to treat long-range electrostatic interactions,[56] with a cutoff of 9 Å and a B-spline interpolation order 4. The electrostatic embedding scheme was used for the QM region adopting a cutoff of 12 Å. The covalent bonds truncated at the interface between the QM and MM regions were replaced with hydrogen link atoms (3 in total).

Each system was relaxed using 500 steps of steepest descent followed by 500 steps of conjugate gradient method with the protein backbone restrained. Afterward, 50 ps of equilibration were carried out in the canonical (NVT) ensemble heating the system from 0 to 303.15 K with a heating rate of ∼ 0.26 K · fs^{-1}. We then performed 100 ps of production run in the NPT ensemble at the pressure and temperatures of 1 bar and 303.15 K, realized with the Berendsen barostat[57] and the Langevin thermostat. The collision frequency and time constant were set to 2 ps^{-1} and 1 ps, respectively, for the Langevin dynamics, while a pressure relaxation time of 1 ps was used for the pressure regulation.

The trajectories were collected adopting a time step of 1 fs and saving the values of the descriptors used for the HLDA procedure each simulation step with the PLUMED 2.9 plug-in.[58] The covalent bonds of the MM region between the hydrogens and either the heavy atoms of the protein, or the oxygen atoms of water molecules, were constrained with SHAKE[59] and SETTLE,[60] respectively.

Well-Tempered QM/MM MD Simulations. Once the optimal CVs were obtained via HLDA, well-tempered metadynamics[38] QM/MM MD simulations were performed to accelerate the sampling and help the system overcome the FE barriers.

In metadynamics,[61] the evolution of the system is based on a potential biased with a history-dependent term $w(s, t)$ that is constructed as a sum of Gaussian functions[62] deposited along the trajectory in the CV-space:

$$w(s, t) = \sum_{\substack{t'=\tau_G,2\tau_G,\ldots,\\ t'<t}} \omega_G e^{-|s(t)-s(t')|^2/2\delta s^2} \quad (1)$$

where s is the CV, ω_G is the height of each Gaussian, τ_G is the size of the time interval between successive Gaussian depositions and δs is the Gaussian width. These repulsive Gaussians are centered at the explored points in the CV-space with a *deposition rate* $\omega = \omega_G/\tau_G$. The biasing energy terms are repeatedly added to the potential to discourage the system from visiting again the already explored configurations, thus ensuring a homogeneous sampling of the CV-space.

In the "well-tempered" variant (WTMD), each Gaussian is scaled down over time by a bias factor $\gamma = e^{\frac{w(s,t)}{k_B \Delta T}}$, which is defined by the value of $w(s, t)$ at the same point where the

https://doi.org/10.1021/acscatal.5c01263
ACS Catal. 2025, 15, 10702−10721

Gaussian is centered, the Boltzmann constant k_B, and a biasing temperature ΔT selected as an input parameter. This procedure determines the deposition of Gaussians with different heights, which depend on the biases already accumulated in the given point of the CV-space.

Here, WTMD was implemented with the PLUMED 2.9 plug-in.[58] Gaussians were deposited with a rate ω = 50, setting the Gaussian height at 5 kJ/mol, δs at 0.05 Å and γ=20.

WTMD QM/MM MD simulations were performed with the *sander* engine implemented in AMBER adopting the same theory level (DFTB3) and setup used for unbiased QM/MM MD simulations. Each reaction step (acylation and deacylation for PETase-PET4 and PETase-PEF4 systems) was simulated for 1000 ps, followed by reweighting of the biased distribution. The reweighting and block analysis were used to monitor the convergence and to calculate the errors in the FE estimation.

Analysis of the Well-Tempered Metadynamics Trajectories. The stationary points corresponding to stable and metastable states along the FE surfaces (local energy minima) obtained from WTMD simulations were characterized by calculating the average values of the structural descriptors of the system. To compute average values from equilibrium distributions, representative structures correlating with minima on the WTMD FE curves were extracted and subjected to 50 ps-long unbiased QM/MM MD simulations adopting the same setup described beforehand for the unbiased simulations.

The fluctuations of the features during these unbiased trajectories were monitored with PLUMED 2.9,[58] and they include the distances and coordination numbers used to optimize the reaction coordinate via HLDA (d1-d11 and c1-c3). Moreover, two further distances (d12 and d13) and two angles (a1 and a2) have been analyzed to assess the stabilization of the carbonyl O_5" atom by the oxyanion hole. The distances d12 and d13 were calculated between the O_5" atom of PET4 or PEF4 and the amide H atom of the M161 and Y87 backbones, respectively, while a1 and a2 correspond to the N−H---O angle formed by the amide N and H atoms of the M161 and Y87 backbones and the O_5" atom of PET4 or PEF4 (Figure S3). Finally, the conformation of the W185 side chain was defined based on the dihedral angle (t1) formed by atoms Cα-Cβ-Cγ-Cδ (Figure S3).

Committor Analysis for the Validation of the Transition State. To assess whether the reaction coordinate obtained via HLDA correctly identified the TS, we performed a committor analysis. From each WTMD trajectory (PET4 and PEF4 acylation and deacylation), we selected one representative structure correlating with the transition states predicted for each reaction stage, i.e., configuration whose HLDA CV value corresponded to the maxima of the FE landscapes.

From each of these structures, we generated an ensemble of TS-like configurations by running 500 fs-long MD simulations under a strong harmonic restraint (k = 5000 kJ/(mol·Å^2)) centered on the HLDA value associated with the TS. These ensembles served as the starting point for the committor analysis.

For each putative TS identified in the FE profiles, we performed 500 independent, unbiased MD simulations (100 fs long each) using the TS ensembles as initial configurations. The probability of the system evolving toward reactants or products was computed as the ratio of trajectories reaching each end point to the total number of simulations.

Calculation of the High-Level Free Energy Curves via MetaFEP. Following the procedure outlined in ref.,[43] the FE curves obtained from WTMD simulations at the DFTB3 level were perturbatively corrected using accurate Hamiltonians via MetaFEP. With this method, a restricted number of configurations (N) are extracted from the WTMD trajectory and used to compute the single-point energies at a higher level of theory. In this way, the low-level FE (FE_{LL}) is used as a reference to reconstruct the target accurate potential (FE_{HL}) by means of FE perturbation (FEP) according to the following relationship:

$$FE_{HL}(s(\boldsymbol{R})) = FE_{LL}(s(\boldsymbol{R})) + \Delta F_{FEP}(s(\boldsymbol{R})) \quad (2)$$

With $s(R)$ representing the CV selected as a function of the Cartesian coordinates of the system represented by vector R. For a detailed description of the calculation of the $\Delta F_{FEP}(s(R))$ term using MetaFEP, please refer to Section S2.

For each low-level WTMD trajectory, we discarded the first 225 ps and extracted one configuration every 0.500 ps for the successive 775 ps, obtaining a total of 1550 structures. For each of them, we calculated the single point energies at the following levels of theory:

- DFT with the PBE functional[63] and the 6−31+G* basis set.[64]
- DFT with the B3LYP[65] functional and the def2-TZVP basis set.[66]
- The second-order many-body Møller−Plesset wave function-based method (MP2)[67] in combination with the resolution of identity (RI) approximation (RI-MP2)[68] using the correlation consistent cc-pVTZ basis set.[69] The RI−JK approximation was used for Coulomb and Exchange integrals with the auxiliary basis set def2/JK.[66,70,71]

Each calculation was performed using AMBER22[51,52] interfaced with ORCA 6.0.[53] Once each single-point SCF run converged, the FE profile was reconstructed using the python script deposited on the PLUMED-NEST repository (www.plumed-nest.org), with plumID:19.054.[43] This python script performs a reweighting analysis based on FEP (eq 2)) using data collected from the single-point calculations performed at DFTB3 level ($FE_{LL}(s(R))$) and at the high level of theory ($FE_{HL}(s(R))$) stored in the same COLVAR file. A detailed description of the procedure is reported in Section S2.

The convergence of the MetaFEP corrections was assessed with the procedure outlined in Section S2 and reported in Figure S4.

Calculation of the Reactivity Indexes from Conceptual DFT. The local relative reactivities of the PET4 and PEF4 were estimated by using the indices defined in the framework of conceptual DFT.[44,72−74] In particular, Chattaraj et al.[75,76] introduced a local (multi)philicity index (ω_k^α), suitable for comparing the electrophilic-nucleophilic relative reactivities of a given atomic site k found on different molecules:

$$\omega_k^\alpha = \omega f_k^\alpha \quad \text{with } \alpha = +, -, 0 \quad (3)$$

where f_k^α are the condensed Fukui functions[77] and ω is the global electrophilicity index.[78] Details on the global reactivity indices and the condensed Fukui functions calculated in this work are reported in Section S3.

According to their definition, a greater ω_k^+ value corresponds to a better capability of accepting electron density, whereas a smaller value of ω_k^- makes it a better donor of electron density.[72] To equalize the notions and to

https://doi.org/10.1021/acscatal.5c01263
ACS Catal. 2025, 15, 10702−10721

obtain a descriptor for local nucleophilicity for which high value corresponds to high tendency at donating electron density, a nucleophilicity index N_k' was proposed as the inverse of ω_k^-:[79]

$$N_k' = \frac{1}{\omega_k^-} \tag{4}$$

In this work, the philicity indices of each atom forming the ester groups of PET4 and PEF4 were calculated and examined to compare the relative reactivities both at the global and local level. Given the well-established dependency of the condensed Fukui functions—formulated in eqs S12 and S13 - on the chosen population analysis scheme,[80−84] four models were selected and compared: the Mulliken,[85] the ChelpG,[86] the Hirshfeld[87] and the minimal basis iterative stakeholder (MBIS)[88] schemes. To compute the condensed Fukui functions, 10 structures were extracted for both PET4 and PEF4 bound to PETase from the unbiased QM/MM MD simulations. As no significant structural changes were observed during the 100 ps of unbiased QM/MM MD simulations, representative structures were selected by uniformly sampling the trajectories at 10 ps intervals, ensuring that the entire time scale was adequately covered. For each configuration, the atomic population of each atom involved in the ester group (C, O', O'', Figure S1) of the neutral system ($Q_k(n)$), for the system with $n + 1$ (eq S12) and the system with $n - 1$ (eq S13) electrons were calculated. In these two latter cases, the multiplicity of the system was two, and the SCF procedure turned to open shell. The calculations were carried out with ORCA[53] at the B3LYP/def2-TZVP level of theory. The HOMO and LUMO energies were extracted from the calculation for the system with n electrons and used to compute the local philicity ω_k^α indices as described in eq 3 and the local nucleophilicity index (N_k') introduced in eq 4). The results and associated errors are reported as the mean and standard error of the mean over the 10 configurations sampled for each substrate.

RESULTS

Reaction's Descriptors Feature Importance Analysis from HLDA. The main advantage of using HLDA is that the definition of the reaction coordinate is not driven by any *a priori* information on the mechanism under investigation, apart from the initial and final states of the process. Indeed, the coefficients of the linear combination indicate the relative weight of each descriptor (feature importance), suggesting how changes in that specific degree of freedom will drive the system toward one of the two end points of the transition. The coefficients obtained by solving eq S1 depend on the scatter matrices S_b and S_w of the distributions collected during the unbiased QM/MM MD simulation, which are shown in Figure S2. The larger the separation between the distributions obtained for the two end points, the greater is the relevance of the descriptor in separating the two states of the system. Conversely, highly overlapping distributions indicate that the descriptor is not significantly different in the two classes and its relative weight in the linear combination will be negligible. Concerning the acylation of the PETase-PET4 system (Figure S2A), it can be observed that the profiles for distances d1, d2, d3, and d6 are neatly separated. For each of these descriptors, one of the two distributions of either the reactant (orange) or the product (blue) is sharp and characterized by a small variance because the atoms considered for these distances are involved in a covalent bond. Conversely, larger fluctuations are observed in the other state, in which these bonds are broken. From the coefficients reported in Table S1, the highest weighted feature is d2 (−0.817), describing the ester bond of PET that is cleaved upon the nucleophilic attack by S160. The second highest-weighted descriptor is d3 (−0.494), that accounts for the distance between the Oγ atom of S160 and the associated Hγ atom (Figure 2). Both these bonds are broken during acylation. Indeed, d2 and d3 have the same sign, meaning that elongation or contraction of these distances drive the system in the same direction along the reaction coordinate. On the other hand, d1 and d6 correspond to bonds that are formed during the acylation step (Scheme 1A). The sign of the coefficients is positive indicating that changes in these distances guide the system toward the opposite end point than d2 and d3.

From the coefficients obtained for the deacylation of the PETase-PET4 acyl-enzyme intermediate (Table S1), it can be observed that d11 is the main driver of the process with a weight of −0.922. This distance accounts for the formation of the new covalent bond between the O atom of water and the C_S atom of PET4. This process is accompanied by a deprotonation of water, whose coordination number (c1) is expected to decrease consistently with d11, thus displaying coefficients with the same sign. The other relevant descriptor of the process is d1 (0.353), that corresponds to the distance between the C_S atom of PET and the Oγ atom of S160 (Figure 2). These atoms form a covalent bond in the acyl-enzyme intermediate, that is broken by the nucleophilic attack of water during the deacylation, with S160 intercepting one proton from water (Scheme 1C). Consequently, the coefficients of d1 and c3 vary in a consistent manner relative to each other and drive the reaction in an opposite direction to d11 and c1. The other descriptors are not relevant in separating the two FE basins of the deacylation step, as the relative distributions overlaps (Figure S2B) and their coefficients in the HLDA CV are close to zero.

As expected, the results obtained for the PETase-PEF4 system (Figure S2C,D) resemble those obtained for PET4. In the acylation step, the highest-weighted descriptors are d2 and d3, while d1 and d6 exhibit opposite signs. Moreover, the contributions of d4, d5, and d8 are more relevant in this system compared to PETase-PET4, although they remain secondary relative to d2 and d3. Finally, as with PET4, the deacylation is predominantly governed by d11, bearing a coefficient of −0.955, followed by d1, which is weighted 0.291.

Reaction Mechanism of PET4 and PEF4 Hydrolysis from Well-Tempered Metadynamics Molecular Dynamics Simulations. The FE profiles of the acylation and deacylation steps were obtained by first applying WTMD along the HLDA reaction coordinate at the DFTB3 level and subsequently calculated using statistical reweighting. To assess the structural properties of the stable and metastable structures produced in course of the reaction, the representative configurations correlating with FE minima were extracted and simulated for 50 ps under the same conditions as those used for WTMD simulations. With this procedure (i) the average properties of these structures were extracted under equilibrium conditions and (ii), it was verified that the metastable states corresponding to putative reaction intermediate are stable in the absence of external biases. The average values of the descriptors calculated with this procedure

https://doi.org/10.1021/acscatal.5c01263
ACS Catal. 2025, 15, 10702−10721

Table 1. Average Values of the Descriptors at the Stable States Visited during the WTMD Simulations[a]

PETase − PET4										
Acylation										
State	d1 (Å)	d2 (Å)	d3 (Å)	d4 (Å)	d5 (Å)	d6 (Å)	d7 (Å)	d8 (Å)	d9 (Å)	d10 (Å)
R	2.80 ± 0.30	1.36 ± 0.03	0.99 ± 0.03	2.08 ± 0.42	1.25 ± 0.02	3.31 ± 0.32	4.86 ± 0.53	2.88 ± 0.23	1.97 ± 0.19	1.03 ± 0.03
$INT_{ac\text{-}enz}$	1.38 ± 0.04	3.50 ± 0.15	3.84 ± 0.23	4.81 ± 0.23	1.24 ± 0.02	0.97 ± 0.03	4.97 ± 0.39	3.00 ± 0.21	1.99 ± 0.18	1.03 ± 0.03
PETase − PEF4										
Acylation										
State	d1 (Å)	d2 (Å)	d3 (Å)	d4 (Å)	d5 (Å)	d6 (Å)	d7 (Å)	d8 (Å)	d9 (Å)	d10 (Å)
R	3.51 ± 0.08	1.35 ± 0.03	0.98 ± 0.03	2.80 ± 0.40	1.25 ± 0.02	3.66 ± 0.25	4.27 ± 0.40	3.24 ± 0.30	1.94 ± 0.16	1.03 ± 0.03
INT_{tetr}	1.47 ± 0.07	1.66 ± 0.14	2.36 ± 0.19	1.06 ± 0.03	1.29 ± 0.03	1.65 ± 0.20	2.72 ± 0.17	3.19 ± 0.15	1.72 ± 0.18	1.06 ± 0.04
$INT_{ac\text{-}enz}$	1.35 ± 0.03	3.24 ± 0.30	3.45 ± 0.15	2.57 ± 0.73	1.26 ± 0.02	0.98 ± 0.03	3.21 ± 0.38	3.40 ± 0.26	1.98 ± 0.19	1.03 ± 0.03
PETase− PET4													
Deacylation													
State	d1 (Å)	d2 (Å)	d3 (Å)	d4 (Å)	d5 (Å)	d6 (Å)	d7 (Å)	d8 (Å)	d9 (Å)	d10 (Å)	d11 (Å)	c1	c2	c3
$INT_{ac\text{-}enz}$	1.36 ± 0.03	4.84 ± 0.51	5.09 ± 0.54	6.15 ± 0.52	1.25 ± 0.02	1.13 ± 0.27	6.67 ± 0.43	2.86 ± 0.18	1.83 ± 0.29	1.06 ± 0.10	3.25 ± 0.35	1.77 ± 0.39	0.62 ± 0.38	0.51 ± 0.21
P	3.56 ± 0.38	3.77 ± 0.24	3.98 ± 0.80	5.04 ± 0.67	1.25 ± 0.02	0.99 ± 0.03	5.04 ± 0.75	3.29 ± 0.38	2.05 ± 0.20	1.02 ± 0.03	1.34 ± 0.03	0.90 ± 0.02	0.55 ± 0.28	1.34 ± 0.24
PETase− PEF4													
Deacylation													
State	d1 (Å)	d2 (Å)	d3 (Å)	d4 (Å)	d5 (Å)	d6 (Å)	d7 (Å)	d8 (Å)	d9 (Å)	d10 (Å)	d11 (Å)	c1	c2	c3
$INT_{ac\text{-}enz}$	1.35 ± 0.03	5.69 0.77	6.05 ± 0.85	4.78 ± 0.91	1.25 ± 0.02	0.99 ± 0.03	4.54 ± 0.81	3.02 ± 0.03	2.02 ± 0.20	1.02 ± 0.03	2.84 ± 0.05	1.80 ± 0.02	0.42 ± 0.11	0.33 ± 0.13
P	2.76 ± 0.01	4.19 ± 0.04	5.44 ± 0.09	4.92 ± 1.16	1.24 ± 0.02	0.98 ± 0.03	4.36 ± 0.64	3.31 ± 0.21	2.01 ± 0.17	1.02 ± 0.03	1.36 ± 0.03	0.96 ± 0.04	0.47 ± 0.10	1.12 ± 0.07

[a]The average value and the associated error of each descriptor are calculated as mean and standard deviation of the equilibrium distributions. These are provided by unbiased QM/MM MD simulations of the representative structures correlating with the FE minima and corresponding with the stable (reactants − R, acyl-enzyme intermediate − INTac-enz, products − P) and metastable (tetrahedral intermediate − INTtetr) states

are reported in Tables 1 and S2, and they are used to support the discussion of the two reaction stages (acylation and deacylation) in the following sections. The definition of each descriptor can be found in Table S1 and illustrated in Figure S1, whereas the relevant atoms are highlighted in Figure 2.

Acylation Stage of PET4 and PEF4 Catalysis. The FE curves obtained for the acylation of PET4 (Figure 3A) and PEF4 (Figure 3C) indicate substantial differences in the underlying mechanisms. The acylation of the PETase-PET4 system occurs through a single, concerted step, in which a FE barrier peaking at ≈ 21 kcal/mol is found at a CV value of ≈ −1.7 (Figure 3A). In the reactant state (R), localized at a CV value of ≈ −0.5, the catalytic S160 and the substrate PET4 do not form covalent bonds (Table 1, d1 = 2.80 ± 0.30 Å, blue region in Figure 3B). When the process starts, the Oγ atom of S160 progressively approaches the ester C_5 atom of PET4 (d1 = 1.53 ± 0.07 Å, green region in Figure 3B). Concurrently, the Oγ-Hγ bond of S160 elongates (d3), and the proton is progressively abstracted by the H237 side chain (d4). The O_5'' atom of PET4 points toward the M161 and Y87 backbones, at distances (Table S2, d12, d13) and angles with the amide N−H groups (Table S2, a1, a2) compatible with the formation of stabilizing hydrogen bonds (HBs), although O_5'' remains farther from M161 (d12) compared to Y87 (d13). At the peak of the FE barrier, a tetrahedral transition state (TS_{r1}) structure is formed. S160 is fully deprotonated, with the Hγ atom being transiently captured by H237. At this stage, the carbonyl O_5'' atom of PET4 has moved closer to the M161 and Y87 backbones, which form the oxyanion hole stabilizing the negatively charged TS. Moving along negative values of the reaction coordinate, the TS evolves toward the product, that is the acyl-enzyme intermediate ($INT_{ac\text{-}enz}$). In this state, the covalent bond between the Oγ atom of S160 and the C_5 atom of PET4 is formed (d1 = 1.38 ± 0.04 Å), whereas the ether C_5−O_5' bond of PET4 is broken (d2 = 3.50 ± 0.15 Å, red region in Figure 3B). At the same time, the Hγ of S160 has been transferred to the O_5' atom of PET4 (d6 = 0.97 ± 0.03 Å), yielding the first product of the catalytic cycle, composed of two PET monomers (PET2'), accompanied by a reaction energy of ≈ 4.8
kcal/mol.

The FE profile obtained for the acylation of the PETase-PEF4 system (Figure 3C) shows substantial differences from that of PET4. In this case, the process is characterized by two energy barriers of ≈ 10 kcal/mol and ≈ 2 kcal/mol at values of ≈ −0.7 and ≈ −2.2, respectively, along the reaction coordinate, in the midst of which a metastable intermediate is observed (green region in Figure 3D). Similarly to PET4 acylation, the reaction starts with the progressive approach of the Oγ atom of S160 to the C_5 atom of PEF4 and the stretching of the O−H bond: d1 decreases (blue region in Figure 3D) and d3 increases. At variance with the PET4 acylation, when the first TS (TS_{r1}) is formed, the serine residue is not fully deprotonated, but the Hγ atom is shared between the Oγ atom of S160 and the Nε atom of H237. Beyond the first FE barrier, at CV values of ≈ −1.7, the system reaches a metastable configuration that correlates with a tetrahedral configuration (INT_{tetr}) in which S160 has transferred the Hγ atom to H237. H237 remains stably protonated (d4 = 1.06 ± 0.03 Å), producing a zwitterionic system with a neat charge

https://doi.org/10.1021/acscatal.5c01263
ACS Catal. 2025, 15, 10702−10721

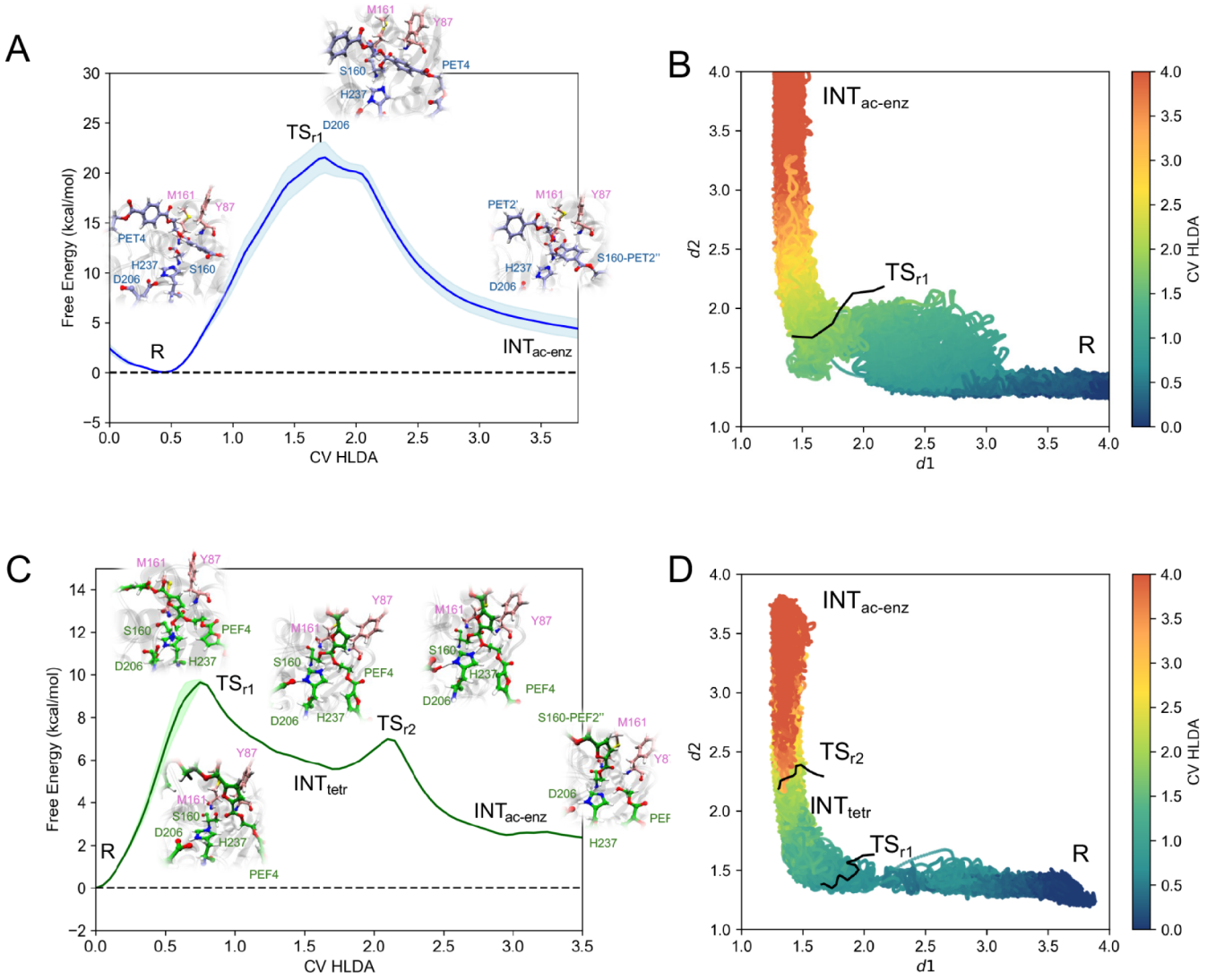

Figure 3. Free energy profiles of acylation calculated from WTMD simulations at DFTB3 level of theory. FE curve for PET4 (**A**) and PEF4 (**C**) acylation calculated along the collective variable (CV) optimized via HLDA. The error associated with each FE curve is estimated from the block error analysis. The sign of the CV was inverted to aid readability of the reaction progress: the reactants (R) on the left and the products (INT_{ac-enz}) on the right. Representative snapshots of each stationary point extracted from the trajectory are shown in correspondence of the related positions along the CV axis. Distribution of the distances corresponding to bonds that is formed (d1) and broken (d2) during the PET4 (**B**) and PEF4 (**D**) acylation. The maps are colored as a function of the HLDA CV value, highlighting the state of the system during the process.

separation: a positively charged H237 and a negatively charged tetrahedral intermediate. In this state, the O_5'' atom forms tighter HBs with the oxyanion hole (Table S2). Interestingly, in the INT_{tetr} state, the D206 carboxylic side chain is closer to the Hδ atom of H237 (d9) compared to the other states in which the imidazole ring is uncharged (R, INT_{ac-enz}). This suggests that the acidic character of D206 activates H237, increasing its basicity and facilitating the deprotonation of S160. Moreover, when the tetrahedral adduct is formed, the dihedral angle of the W185 side chain slightly decreases of ≈ 10°, on average, compared to that found for the other states of the reaction (Table S2, t1 = 85.97 ± 11.04). The subtle kink of the tryptophane side chain helps the ester group of the substrate to move closer to the S160 and to correctly position the carbonyl moiety within the oxyanion hole. At greater values along the HLDA CV axis, INT_{tetr} evolves toward the product overcoming the second FE barrier, that is only ≈ 2 kcal/mol high. At this second FE maximum, the new bond between the Oγ atom of S160 and the C_5 atom of PEF4 is established and the ether bond between C_5 and O_5' is stretched, but not yet completely broken. Beyond this second energy hill, INT_{ac-enz} is formed (red region in Figure 3D), with the complete cleavage of the $C_5 - O_5$' bond (d2 = 3.24 ± 0.30 Å) and the protonation of the O_5' atom (d6 = 0.98 ± 0.03 Å) by H237 which, in turn, slightly displaced from D206 (d9 = 1.98 ± 0.19 Å). This process yields the first leaving molecule of the catalytic cycle (PEF2'), with an associated reaction energy of ≈ 2.5 kcal/mol, thus resulting in less endergonic than the acylation of PET4.

Deacylation Stage of PET4 and PEF4 Catalysis. The deacylation of the acyl-enzyme intermediates produced during the first step of the catalytic cycle occurs following the entry of a water molecule within the active site. This process is triggered by the nucleophilic attack of the water molecule on the S160-substrate adduct, yielding the final product of the catalysis and restoring the enzyme to its initial state. The deacylation of the S160-PET2'' intermediate (Figure 4A, INT_{ac-enz}) starts with the PET2'' fragment stably bound to the

https://doi.org/10.1021/acscatal.5c01263
ACS Catal. 2025, 15, 10702−10721

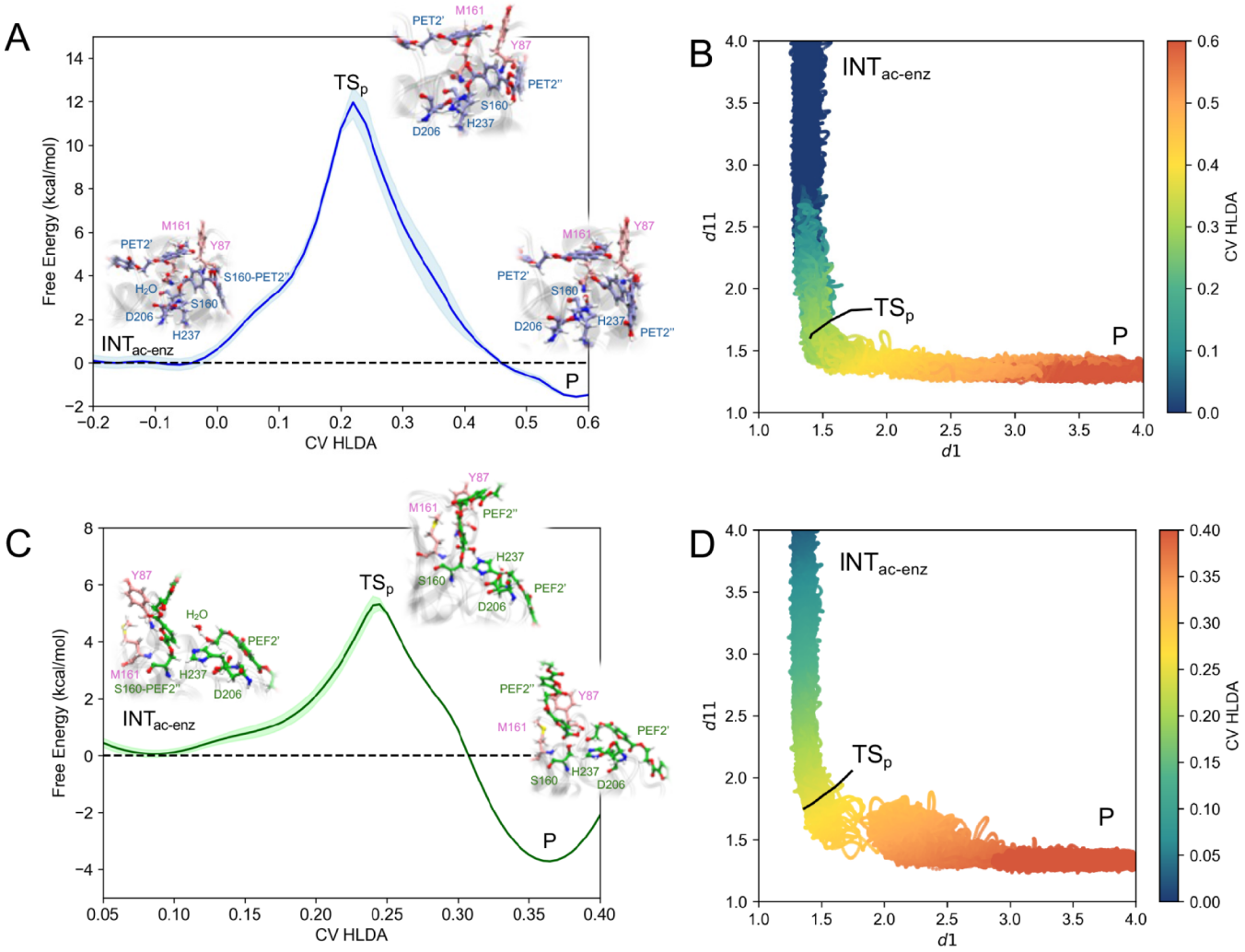

Figure 4. Free energy profiles of deacylation calculated from WTMD simulations at DFTB3 level of theory. FE curve for PET4 (**A**) and PEF4 (**C**) deacylation calculated along the collective variable (CV) optimized via HLDA. The error associated with each FE curve is estimated from the block error analysis. Representative snapshots of each stationary point extracted from the trajectory are shown in correspondence of the related positions along the CV axis. Distribution of the distances corresponding to bonds that are formed (d1) and broken (d11) during the PET4 (**B**) and PEF4 (**D**) deacylation. The maps are colored as a function of the HLDA CV value, highlighting the state of the system during the process.

serine side chain (Table 1, d1 = 1.36 ± 0.03 Å, blue region in Figure 4B). The first product of the catalysis obtained during acylation (PET2') has slightly shifted away from the active site (d2 = 4.84 ± 0.51 Å), leaving room for the water molecule to move closer to the catalytic site (d11 = 3.25 ± 0.35 Å). At this stage, the two H atoms of water are mainly coordinated by the water O atom (c1 = 1.77 ± 0.39), with only transient contacts with H237 (c2 = 0.62 ± 0.38) and S160 (c3 = 0.51 ± 0.21). As the reaction progresses, the water O atom moves closer to C_5 atom of the S160-PET2'' system, with the concurrent elongation of the Oγ − C_5 bond. At the peak of the FE barrier, reached at a value of ≈ 12 kcal/mol, a tetrahedral transition state (TS$_p$) is formed (green region in Figure 4B). Near the TS$_p$ state, the water O atom coordinates only one H atom, with the second proton shared between H237 and S160. During the transition from INT$_{ac-enz}$ to TS$_p$, the carbonyl O_5'' atom remains coordinated with the M161 and Y87 backbone amide groups. Beyond the FE barrier, the system evolves toward the second product of the catalysis (PET2''). Once the second energy minimum is reached (P), the Oγ − C_5 bond is broken (d1 = 3.56 ± 0.38 Å, red region in Figure 4B) and the S160 side chain has restored its initial active state capturing one H atom of water (c3 = 1.34 ± 0.24). On the product side, the O atom of water has bound the C_5 atom (d11 = 1.34 ± 0.03 Å) carrying the second H atom (c1 = 0.90 ± 0.02) and yielding the last leaving molecule of the process (PET2''). Globally, this stage is mildly exergonic, with a reaction energy of ≈ − 1.7 kcal/mol. Akin to PET deacylation, the hydrolysis of the S160-PEF2'' adduct occurs in a concerted manner (Figure 4C), visiting one single TS (TS$_p$) peaking at ≈ 5 kcal/mol. On the reactants side (R), the Oγ − C_5 bond of INT$_{ac-enz}$ is stable (Table 1, d1 = 1.35 ± 0.03 Å, blue region in Figure 4C), with the water O atom in proximity to the target C_5 atom (d11 = 2.84 ± 0.05 Å) but still binding both H atoms (c1 = 1.80 ± 0.02). Moving uphill toward the TS, the Oγ − C_5 bond starts stretching whereas the water O atom approaches the C_5 atom of PEF2''. Near the top of the FE barrier, TS$_p$ exhibits a tetrahedral geometry, with the O_5'' atom aligned with the N−H group of M161 and Y87 (green region in Figure 4B). Finally, beyond the FE hills, the product (P) is formed. At the second FE basin, the Oγ − C_5 bond is cleaved (Table 1, d1 = 2.76 ± 0.01 Å, red region in Figure 4B) and S160 side chain

https://doi.org/10.1021/acscatal.5c01263
ACS Catal. 2025, 15, 10702−10721

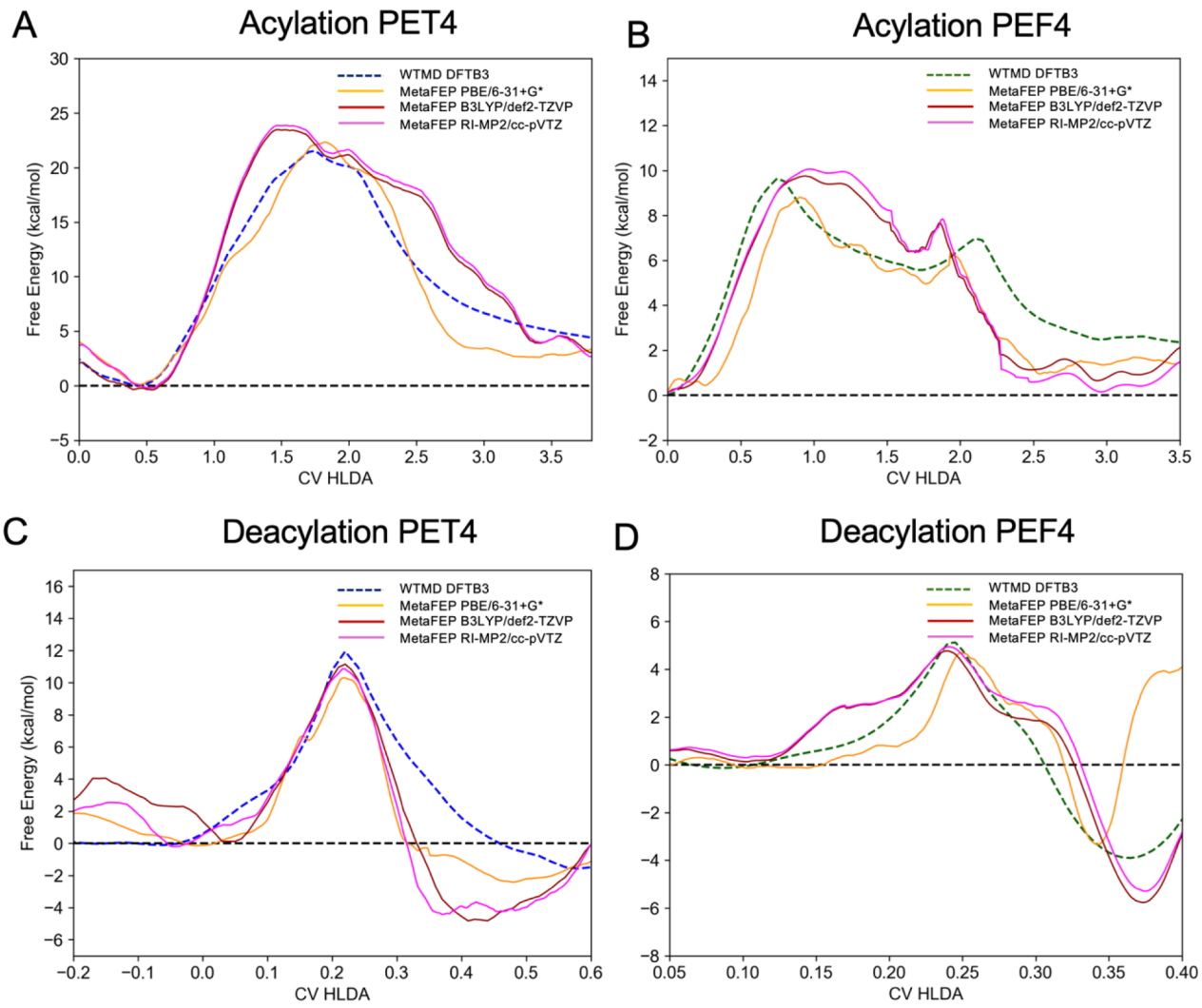

Figure 5. Free energy curves of acylation and deacylation obtained via MetaFEP. The FE profiles of (**A**) PET4 and (**B**) PEF4 acylation and (**C**) PET4 and (**D**) PEF4 deacylation have been optimized via MetaFEP by using those obtained at the DFTB3 level as a reference. The results obtained with the PBE, B3LYP and RI-MP2 Hamiltonians are shown as solid orange, red and magenta lines, respectively. The DFTB3 curves are shows as dashed blue and green lines for PET4 and PEF4 reaction steps, respectively.

abstracted one H atom from water (c3 = 1.12 ± 0.07). This, in turn, becomes bound to C_5 (d11 = 1.36 ± 0.03 Å), yielding the second product of the catalysis (PEF2") with a reaction energy of ≈ − 3.8 kcal/mol, making it approximately twice as exergonic as the S160-PET2" deacylation.

The Committor Analysis Confirms the Identities of the Transition States. To assess whether reaction coordinate obtained via HLDA correctly identified the TS visited during each reaction step, we performed a committor analysis. The committor probability is the fraction of trajectories initiated from a given point of the FE surface with Boltzmann distributed velocities that commit to the product basin.[34,89] Therefore, by definition, the committor probability takes the value of 1 for the products, 0 for the reactants and 0.5 for the TS.[34] In order to validate the correct assignment to the TS by the HLDA variable, we selected one representative structure for each FE peak of each reaction stage shown in Figures 3 and 4. From each of these structures, we generated a TS ensemble of configurations with the procedure described in the Computational Methods, which served as a starting point for the committor analysis. Each structure was left evolving toward one metastable basin of the FE landscape via unbiased MD simulations, and the distributions of the final end points (reactant or products) were characterized via their position along the HLDA CV axis, as shown in Figure S6. From this analysis, it can be observed that the probability that the system, starting from the putative TS ensemble, evolved toward either the reactant (orange distributions) or the product (blue distributions) of each reaction step is ≈ 0.5, confirming the correct identification of the saddle points onto the FE curves. Furthermore, it is worth noting that the product-side distribution obtained starting from TS_{r1} (Figure S6B) and the reactant-side distribution obtained starting from TS_{r2} (Figure S6C) of PEF4 acylation peak at values between 1.5 − 1.6 along the HLDA CV axis. This range corresponds to the metastable basin identifying the INT_{tetr} state, further validating the multistep nature of the PEF4 acylation predicted by our WTMD simulations (Figure 3C).

High-Level of Theory Mechanism Validation via MetaFEP. After achieving convergence in the DFTB3 WTMD simulations, configurations were sampled from each trajectory following the protocol outlined in the Computational Methods. For each structure, the single-point energies were calculated at the PBE, B3LYP and RI-MP2 levels and

https://doi.org/10.1021/acscatal.5c01263
ACS Catal. 2025, 15, 10702−10721

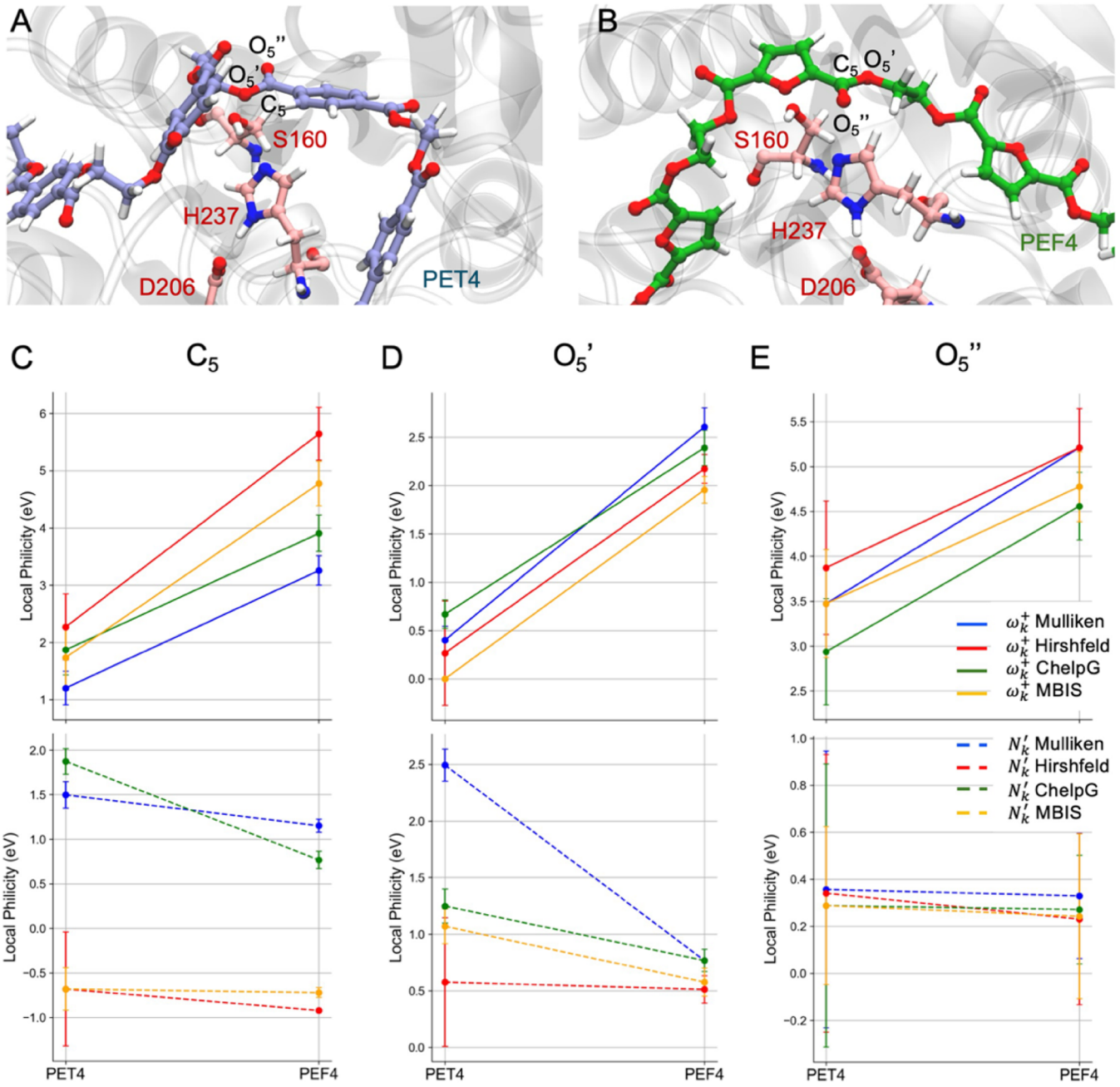

Figure 6. Local philicity indexes of the hydrolyzed PET4 and PEF4 ester group. The atoms of the ester group hydrolyzed during the WTMD simulations are shown for (**A**) PET4 and (**B**) PEF4. The condensed Fukui functions used to compute the local reactivity indices were calculated from four different partitioning schemes at the B3LYP/def2-TZVP level: Mulliken (blue), Hirshfeld (red), ChelpG (green) and MBIS (orange). The variation of the reactivity indexes of the (**C**) C_5, (**D**) O_5' and (**E**) O_5'' atoms from PET4 (left side of each panel) to PEF4 (right side of each panel) is shown as solid lines for the local electrophilicity (ω_k^+) and dashed lines for the local nucleophilicity (N_k^-). The value of each index and the associated errors are reported as mean and standard error of the mean calculated over the data calculated for the ten representative structures sampled for each substrate.

used to reconstruct the corresponding FE curves by applying MetaFEP.[43] The resulting profiles are reported in Figure 5 with the reference DFTB3 FE profiles represented as dashed (blue or green) lines, and the PBE, B3LYP and RI-MP2 FE curves depicted as orange, red and magenta solid lines, respectively. The energy barriers associated with PET4 acylation (Figure 5A) obtained at DFTB3 and PBE levels exhibit remarkable agreement, with maxima positioned at ≈ 1.7 along the HLDA reaction coordinate and reaching heights of ≈ 21 and ≈ 22 kcal/mol, respectively. Higher free energy (FE) barrier values are observed for the RI-MP2 and B3LYP calculations, which show nearly overlapping profiles with maxima of approximately 24 kcal/mol located around 1.3 along the CV axis. Furthermore, on the product side, the FE profiles obtained with these higher-level methods exhibit a more gradual decline compared to those from DFTB3 and PBE. As a result, the basin corresponding to the $INT_{ac\text{-}enz}$ state is reached only at ≈ 3.5 along the HLDA reaction coordinate axis for RI-MP2 and B3LYP calculations, contrary to the DFTB3 and PBE curves, which become flat at a CV value ≈ 3.0. The $INT_{ac\text{-}enz}$ is formed

https://doi.org/10.1021/acscatal.5c01263
ACS Catal. 2025, 15, 10702−10721

at a relative FE of ≈ 4.8 kcal/mol according to DFTB3 calculation, while a plateau at ≈ 2 kcal/mol is observed in the PBE curve. Instead, the local minima obtained at RI-MP2 and B3LYP levels are positioned between those observed in the other two curves, with minimal values at ≈ 3 kcal/mol. Similar trends are observed for PEF4 acylation (Figure 5B), for which a first, sharp FE maximum ≈ 10 kcal/mol high is found at a CV value ≈ 0.7 for the DFTB3 and PBE curves, while the barrier observed at the RI-MP2 and B3LYP levels are broader and ≈ 1 kcal/mol higher. The second FE barrier ≈ 2 kcal/mol high is found at ≈ 2.2 Å along the DFTB3 curve, that is slightly shifted at lower values in the PBE (CV ≈ 2.0) and RI-MP2 and B3LYP (CV ≈ 1.8) profiles. All calculations, therefore, support the presence of a metastable intermediate, positioned at approximately the same coordinate along the HLDA CV axis (≈ 1.6−1.7) across all four FE curves. However, while the local minima in which the INT_{tetr} state is found is broad and shallow for the DFTB3 and PBE calculation, a more localized and narrower basin is observed for RI-MP2 and B3LYP ones. This difference indicates a more rigid and well-defined structure for the metastable state predicted by the two higher levels of theory compared to the broader conformational space sampled with DFTB3 and PBE. Other significant differences are observed in the region corresponding to the formation of the $INT_{ac\text{-}enz}$ state, with the PBE, RI-MP2 and B3LYP calculations exhibiting reaction energies of ≈ 1.0−1.5 kcal/mol, against the ≈ 2.5 kcal/mol estimated by DFTB3, suggesting that the process is slightly less endergonic than how predicted from WTMD simulations.

Considering the deacylation stages, the results obtained for PET4 (Figure 5C) indicate a remarkable consistency in shape, height and position of the FE maxima across each method applied to perform the analysis, with a barrier peaking at ≈ 10−11 kcal/mol at a reaction coordinate of 0.2. However, notable differences are found in the reaction energy of the process. DFTB3 calculations yield minimal value of ≈ − 1.7 kcal/mol, which is only ≈ 0.5 kcal/mol lower than that predicted at the PBE level. In contrast, the reaction energies obtained from RI-MP2 and B3LYP calculations are significantly lower, ≈ − 5.0 kcal/mol, indicating that the process is substantially more exergonic.

Finally, the FE curves calculated for the PEF4 deacylation (Figure 5D) show some discrepancies among the four methods. Each level of theory supports the single-step nature of the process, positioning a ≈ 5 kcal/mol high FE barrier at ≈ 0.24 along the reaction coordinate, but the RI-MP2 and B3LYP energy walls show two shoulders, symmetrically positioned at CV values ≈ 0.17 and 0.30 relative to the central peak. Although the two regions around ≈ 0.16−0.20 and ≈ 0.26−0.30 along the CV axis are not associated with the formation of distinct intermediate states—since no saddle points are observed—they still suggest a high degree of conformational flexibility and the absence of substantial energetic barriers, as they take place over a relatively flat FE surface.

Regarding the reaction energy of the process, the DFTB3 calculations predict a value of ≈ − 4.0 kcal/mol, matched by the PBE results. In contrast, deeper minima are found at the RI-MP2 and B3LYP levels of theory, reaching values of ≈ − 6 kcal/mol and indicating, similarly to PET4 deacylation, a more exergonic nature of the process.

Overall, despite expected quantitative variations in reaction energies and barriers across different levels of theory, the mechanistic hypothesis remains consistently validated. This reinforces the reliability of our considerations and provides deeper insight into the intricacies of this complex catalytic process.

Estimation of PET4 and PEF4 Nucleophilicity and Electrophilicity from Conceptual DFT. The FE profiles obtained from DFTB3 WTMD simulations and at higher theory levels via MetaFEP indicate that the nucleophilic attack by the S160 hydroxyl group occurs more easily on PEF4 compared to PET4. To provide an explanation to this evidence from an atomistic perspective, we based on the principles of conceptual DFT.[73,90] A first estimation of the overall chemical behaviors of the two substrates is given by the calculation of the global descriptors (χ, η, ω) defined from the frontier molecular orbital energies (ϵ_{HOMO}, ϵ_{LUMO}) and reported in Table S3. This analysis predicts an electronegativity (χ) for PEF4 ≈ 1 eV higher than that of PET4, thereby suggesting higher attractivity toward electrons. On the other hand, a higher chemical hardness (η) is found for PET4, indicative of lower polarizability and susceptibility to remodeling of its electron density. These two descriptors were used to estimate the global electrophilicity index (ω), which results ≈ 40% lower for PET4 (133.522 eV) compared to that found for PEF4 (217.073 eV).

In addition, to provide a finer insight into the relative reactivities of the two substrates, we calculated the local reactivity indices for each atom forming the eight ester groups of the two oligomers (k = C, O' and O'', Table S4 for PET4, Table S5 for PEF4). In particular, the local electrophilicity ω_k^+ and nucleophilicity N_k' reflect the tendency of each atom at accepting (ω_k^+) or donating (N_k') electron density, and they depend on a global descriptor (ω) and the condensed Fukui functions (f), as detailed in the Computational Methods section. The atomic populations for the nucleophilic (f^+) and electrophilic (f^-) Fukui functions were calculated at the B3LYP/def2-TZVP level using four different atomic population schemes: Mulliken, ChelpG, Hirshfeld, and the minimal basis iterative stockholder (MBIS). In Figure 6, we present the results obtained for C_5, O_5', and O_5'' atoms for PET4 (panel **A**) and PEF4 (panel **B**), as these atoms form the ester group hydrolyzed during the WTMD simulations. To illustrate the variation between the two substrates, we used uniformly continuous lines for ω_k^+ and dashed lines for N_k' (Figure 6C-E). The results indicate that the ω_k^+ indices of each atom are between 2 to 3 eV higher than those found for PEF4 for each population scheme used to perform the analysis, suggesting that the ester group is significantly more electrophilic in PEF4 than PET4.

Looking at the intramolecular local reactivity of the three atoms of each substrate, the ω_k^+ index of O_5'' seems the highest among in PET4, with values comprised between ≈ 3 − 4 eV, against those of ≈ 1.5 − 2.5 eV obtained for C_5. This difference is attenuated in PEF4, for which the electrophilicity index of C_5 is in the range between ≈ 3.2 − 5.5 eV, while that of O_5'' is ≈ 4.5 − 5.2 eV. Finally, the nucleophilicity of the O_5' is the lowest in both substrates, although it increases by ≈ 4 times in PEF4 compared to PET4, consistent with the trend observed for the entire group. However, it is worth noting that the increase of ω_k^+ from PET4 to PEF4 observed for C_5 (≈ 3

https://doi.org/10.1021/acscatal.5c01263
ACS Catal. 2025, 15, 10702−10721

eV on average) is significantly larger than that found for O_5" (≈ 2 eV on average) and O_5' (≈ 1.5 eV on average).

Opposite drift is found for the nucleophilicity indices N_k' of each atom considered for the analysis, which decreases, albeit to varying degrees, from PET4 to PEF4 across all population analysis models. However, the negative values yielded by the Hirshfeld and MBIS schemes for C_5 (Figure 6C) are indicative of a negligible nucleophilic character for this atom, whereas the N_k' values obtained for O_5" do not vary significantly between the two substrates (Figure 6E). Conversely, the N_k' of O_5', comprised between ≈ 0.5−2.5 eV in PET4, is subjected to an evident decrease in PEF4, reaching values between ≈ 0.5−0.8 eV across all calculations (Figure 6D).

The values of f^+, f^-, ω_k^+ and ω_k^- for each C, O' and O" atom of PET4 and PEF4 are reported in Table S4 and Table S5, respectively, and the pattern discussed in this paragraph is globally consistent in each ester moiety of the substrates. To assess the impact of the enzymatic environment on substrate reactivity, we extended the local philicity analysis to an ester group located away from the catalytic site. Specifically, we examined atoms C_2, O_2', and O_2" in PET4 and PEF4, shown in Figures S7A and S7B, respectively. This group was selected because (i) it is situated far from the PETase active site, (ii) it retains the same chemical connectivity as the catalytically relevant ester group (C_5, O_5', O_5"), and (iii) it is primarily exposed to the solvent bulk. The analysis of the local reactivities performed for the C_2, O_2' and O_2" group shows the same trend as that observed within the catalytic cleft (C_5, O_5', O_5"), with the electrophilicity (ω_k^+) increasing and the nucleophilicity (N_k') decreasing when moving from PET4 to PEF4 (Figure S7C). Interestingly, this variation is particularly pronounced for the O_2" atom, whose ω_k^+ increases by ≈ 5 eV, on average, in contrast to the ≈ 2 eV observed for O_5" (Figure 6E). Since O_5" is embedded within the oxyanion hole of the PETase binding site, we hypothesize that the HBs formed with the Y87 and M161 backbones might reduce its electrophilic character compared to O_2". Indeed, in PEF4, ω_k^+ is comprised between 4.5 and 5.2 eV inside the binding site (O_5"), while it is comprised between 6.8 and 9.0 eV in the solution bulk (O_2"). As a result, the ratio of the relative reactivity indexes between the C atom and the O atom of the carbonyl moiety ($\omega_k^+C_5/\omega_k^+O_5$") is ≈ 0.84 inside the binding pocket, while ($\omega_k^+C_2/\omega_k^+O_2$") ≈ 0.68 in solution, highlighting a shift in the local electronic distribution that favors nucleophilic attack on the carbon atom within the enzymatic environment. This variation is less significant in PET4, for which the relative ω_k^+ ratios are ≈ 0.52 inside the binding site and ≈ 0.49 in solution.

DISCUSSION

The results obtained from the QM/MM simulations of the reaction mechanism of PET4 and PEF4 hydrolysis by PETase elucidate distinctive hallmarks that closely align with the experimental evidence,[13,14] offering a finer mechanistic understanding with molecular detail. A first calculation of the FE profiles was performed at the DFTB3 level via WTMD simulations along the reaction coordinate obtained via HLDA. Our results showed that the acylation stage of PET4 proceeds through one single concerted step, crossing a FE barrier ≈ 21.0 kcal/mol high, and forming an acyl-enzyme intermediate with a reaction energy of ≈ 4.8 kcal/mol. The PET4 deacylation proceeds in a concerted manner as well, with activation and reaction energies of ≈ 12 kcal/mol and −1.7 kcal/mol, respectively, thus suggesting that the acylation is the rate-limiting step of the mechanism. These results agree both qualitatively and quantitatively with the umbrella sampling simulations performed at the PBE and DFTB3 level by Jerves et al.[28] and García-Meseguer et al.,[32] respectively. However, in the work of Burgin et al.,[30] the FE barrier associated with the deacylation results ≈ 2 kcal/mol higher than that of the acylation, leading the authors to identify the acyl-enzyme breakdown as rate-limiting step of the process. A similar conclusion was reached by Dos Santos et al.,[31] who obtained a barrier of ≈ 20 kcal/mol for deacylation after *a posteriori* correction of semiempirical AM1 calculation at the M06−2X level.

The kinetic measurements performed for PET hydrolysis at 30 °C by PETase reported reaction rate constants k_d = 0.8 ± 0.0 s^{-1} and 1.5 ± 0.5 s^{-1} for amorphous films and crystalline powders, respectively.[91] Leveraging the Eyring equation derived from the transition state theory (TST),[92] these values roughly correspond to activation energies of 18 kcal/mol. While the slight discrepancies might be due to the inherent structural differences in the substrates used in the experimental setting (multichain PET samples) and computational studies (single, short PET chain), this value is globally consistent with the FE barriers obtained in this and some previous[28,30−32] works. Moreover, our data, support the hypothesis that the acylation is the slowest stage of the reaction mechanism.[28,32]

In light of the agreement between the results obtained for PET4 with those previously reported with similar levels of theory,[28,32] our approach was extended to the investigation of the reaction mechanism of PEF4 hydrolysis, for which detailed computational investigations are currently lacking in the literature. The FE curves obtained along the HLDA coordinates for the PEF4 hydrolysis are characterized by barriers of ≈ 10 kcal/mol and ≈ 5 kcal/mol for the acylation and deacylation steps, respectively. Therefore, akin to PET4 hydrolysis, the acylation remains the rate-limiting step of the process. On the other hand, at variance of the PET4 acylation, the formation of the PEF4 acyl-enzyme intermediate occurs through two steps: beyond the first FE barrier, a metastable tetrahedral intermediate is formed, which evolves toward the products after a second energy wall ≈ 2 kcal/mol high is overcome.

This shape was confirmed by the PBE-level FE profiles calculated via MetaFEP and represents a crucial difference from PET4, indicating not only that the nucleophilic attack of S160 to the PEF4 ester group occurs faster than PET4, but also that a metastable tetrahedral intermediate is formed. Interestingly, upon formation of the negatively charged tetrahedral intermediate, the dihedral angle (t1) that defines the W185 side chain conformation decreases by approximately 10° compared to the average values observed in other reaction states. Although this shift is moderate, the subtle kink in the indole ring of W185 reflects the transition between two distinct states—referred to as conformation "B" (t1 < 90°) and conformation "C" (t1 > 90°)[27]—characterized previously both experimentally from the crystal structure PDB ID: 5XG0[17,93] and computationally from MD simulations.,[27,30,94] Through this dynamic rearrangement, known as W185 *wobbling*,[17,93] the tryptophan side chain in conformation "B" engages in T-stacking interactions with the aromatic rings of the substrate, facilitating the proper positioning of the ester group within the binding pocket. Then, the bending of the W185 side chain

https://doi.org/10.1021/acscatal.5c01263
ACS Catal. 2025, 15, 10702−10721

toward the substrate and the transition to the "C" conformation promote the approach of the ester carbon atom toward the S160 side chain and enables the carbonyl group to be accurately accommodated within the oxyanion hole.

By applying MetaFEP, we pushed further the accuracy of the Hamiltonian employed to calculate the energetics accompanying the reaction using a wave function-based post-HF method (RI-MP2) and the popular DFT hybrid functional used for the description of organic molecules (B3LYP). Remarkably, these calculations produced almost identical FE curves, characterized by barriers of height compatible with those observed at the DFTB3 and PBE levels. Nevertheless, contrary to DFTB3 results, the sharp and localized FE minima obtained from high-levels calculations (RI-MP2, B3LYP) suggest well-defined and rigid structures for the tetrahedral intermediate states obtained during PET4 and PEF4 acylation. Moreover, more negative energy differences were found for the products of both acylation and deacylation steps. This finding has relevant implications on the thermodynamics of the entire catalytic process. Indeed, according to DFTB3 calculations, the PET4 hydrolysis by PETase results slightly endergonic (+ 4.8 kcal/mol for acylation, − 1.8 kcal/mol deacylation). In contrast, the overall thermodynamic cycle for PEF4 hydrolysis is exergonic (+ 2.5 kcal/mol for acylation, − 3.8 kcal/mol for deacylation). Similar outcomes are provided by the PBE-level MetaFEP correction. On the other hand, the RI-MP2 and B3LYP calculations predict a reaction energy for PET4 acylation and deacylation of ≈ + 3 kcal/mol and ≈ − 5.5 kcal/mol, respectively, reversing the overall thermodynamic balance of the process compared to DFTB3. Concerning PEF4, the high-level calculations provided reaction energies of ≈ + 1 kcal/mol and ≈ − 6 kcal/mol for acylation and deacylation, respectively, thus resulting significantly more exergonic than how predicted with DFTB3 (and PBE).

In spite of the aforementioned differences, the high-accuracy calculations corroborated the mechanistic peculiarities of the PEF4 depolymerization obtained at the DFTB3 level, showing that the acylation proceeds with the formation of a metastable intermediate and this remains the rate-limiting step of the process. Moreover, the FE barriers and the reaction energy of the entire process obtained for PEF4 are lower than those obtained for PET4 for each level of theory considered, indicating that the PEF depolymerization is *both* kinetically and thermodynamically favored.

A possible explanation to this latter evidence is provided by the principles of conceptual DFT to compute key descriptors of the global and local reactivities of the two substrates.[44,72] The global indices describing the electronegativity (χ), the chemical hardness (η) and the electrophilicity (ω), suggested that PEF4 is more likely to accept additional electronic charge from the enzymatic environment. A deeper insight into in the local reactivities of the two substrates was given by the local electrophilicity (ω_k^+) and the local nucleophilicity (N_k') defined from the condensed Fukui functions.[78,90] These descriptors are sensitive to the method used to compute the atomic charges because of the inherent arbitrariness in density partitioning when defining an atom in a molecule.[80−84] Moreover, a further factor that affects the estimation of the Fukui functions is the extension of the basis set. Indeed, the assessment of the local reactivities of the carbonyl group in different molecules conducted in the framework of the B3LYP theory showed some discrepancies among various atomic charge schemes dependent on the chosen basis set, with ChelpG being the only, notable exception.[84] For these reasons, to mitigate the impact of any single method's limitations and provide a more robust understanding of reactivity patterns, it is advisible to select different partitioning schemes to conduct this analysis.[80]

From this standpoint, we compared the local reactivity indexes condensed over the atoms by means of the Fukui functions obtained via the Mulliken, ChelpG, Hirshfeld and MBIS methods, obtaining highly correlated patterns, descriptive of the different reactivity of the ester moieties in the two plastic chains. The increase of the ω_k^+function observed in PEF4 compared to PET4 indicate that ester group is more susceptible to the nucleophilic attack when located next to the furan ring rather than benzene. This variation is particularly evident for C_S, which is the atom of the ester group whose electrophilicity increases more in PEF4 compared to PET4. This evidence is due to its inherently lower electronegativity compared to the two other O atoms and the proximity to the electron-withdrawing furan group. Together, these factors enhance the susceptibility of C_S in PEF4 to nucleophilic attack by the S160 catalytic residue of PETase. Conversely, the decrease of the N_k' function found for PEF4 suggests that this system is less reactive toward electrophilic reagents. This evidence explains the enhanced stability of the tetrahedral adduct formed upon S160 binding and its existence as a metastable intermediate. Indeed, we hypothesize that, in this state, the negative charge is more effectively delocalized in PEF4 compared to PET4. Furthermore, the ether O atom (O_S') in PEF4 is less prone to abstract the proton from the H237 histidine ring, which is the step that triggers the expulsion of the leaving group of the acylation and the formation of the acyl-enzyme intermediate. This characteristic is likely due to the electron-withdrawing effect of the O atom of furan, that forms a dipole across the five-membered ring and depletes the ester moieties of part of the electron density.[95]

In addition to the efficient catalysis, in our previous work[27] we showed that PEF4 tends to dissociate quickly from the PETase binding pocket compared to its counterpart. The combination of the fast hydrolysis of PEF chains with the low residence time of the products of depolymerization points to a high turnover rate for the catalytic cycle, offering a valuable mechanistic description of the enhanced performance observed for PETase against PEF compared to its native substrate. Indeed, experimental findings obtained for macroscopic PEF and PET coupons depolymerization by PETase[13] showed that, after 96 h of incubation of the two polymers with the enzyme, the surface morphology of PEF resulted substantially more modified than that of PET. This observation was corroborated by differential scanning calorimetry (DSC) analysis, that showed a reduction in terms of relative crystallinity of 15.7% for PEF compared with the relative reduction of 10.1% for PET.[13]

Furthermore, recent analysis of Nano-PEF degradation by PETase showed that the WT enzyme is even more efficient than some popular variants engineered so far,[22,25] which, in contrast, demonstrated highest catalytic activity toward PET.[14] This finding can be ascribed to the stiffer active site that characterizes these mutants. While a rigid binding pocket enhances the thermostability of the enzyme, it also compromises the accommodation of the PEF chains, which are less flexible than those of PET because of the polarity of

https://doi.org/10.1021/acscatal.5c01263
ACS Catal. 2025, 15, 10702−10721

the furan ring and the nonlinear axis along which the aromatic ring is connected to the EG.[95]

On the other hand, other variants derived from PETase (FastPETase,[20] TurboPETase[26] and the homologous LCC (LCC^{ICCG})[24,96] outperformed the WT enzyme in PET degradation and also demonstrated remarkable activity toward PEF.[14,97] In line with the previous hypothesis, it is supposed that these enzymes retain a certain degree of the flexibility of the binding grooves,[26,98] thus enabling remodeling of the catalytic domain to favor the accommodation of a broader range of substrates. Therefore, future engineering of these biocatalysts may be directed not only toward enhancing their performance in PET depolymerization, but also expanding their versatility toward other plastic materials.

CONCLUSIONS

In this study, we introduce a robust computational protocol to investigate the reaction mechanism underlying the enzymatic degradation of PET and PEF by PETase, providing a molecular-level explanation for the experimentally observed enhanced activity toward PEF.

The reaction mechanism is explored along agnostically designed reaction coordinates derived via harmonic linear discriminant analysis (HLDA), which requires no prior assumptions about the mechanism beyond the end point states, allowing the inclusion of any relevant chemical modes. QM/MM well-tempered metadynamics (WTMD) simulations are performed at the DFTB3 level, enabling extensive configurational space sampling and the calculation of FE profiles associated with both the acylation and deacylation steps, based on statistically significant distributions.

The energy barriers calculated for PET4 hydrolysis demonstrate remarkable agreement with previously published values,[28,32] underscoring the reliability of our protocol and its applicability to PEF4. Our results reveal distinct mechanisms between PEF4 and PET4 acylation. Unlike PET4, PEF4 acylation follows a two-step process, with the first FE barrier being approximately 10 kcal/mol lower than that observed for PET4. Conversely, the deacylation of both PET4 and PEF4 is concerted, with PET4 exhibiting an energy barrier roughly twice as high as that of PEF4. This mechanistic description is supported by FE profiles calculated at higher levels of theory (PBE, B3LYP, RI-MP2) using MetaFEP, reinforcing the quantitative significance of our findings.

Finally, an atomistic description of the higher reactivity of PEF is provided by conceptual DFT: both global and local electrophilicity indexes suggested that PEF chains are more susceptible to nucleophilic attacks and less prone to donate electron density.

Overall, by posing a kind of "molecular microscope" on the enzymatic depolymerization of two materials, in this work, we capture the atomistic details that differentiate their reaction mechanisms. Our findings lay the groundwork to improve the efficiency of biotechnological tools aimed at upcycling these materials, which will play again pivotal roles in the plastics industry in the coming decades, offering valuable insights into the development of more effective strategies in plastic recycling and sustainability.

ASSOCIATED CONTENT

Data Availability Statement

All QM/MM MD simulations were produced with AMBER (https://ambermd.org). The software is released in two parts: AmberTools and Amber. AmberTools package is freely available and released under the GNU General Public License (GPL). Amber package is granted under license and released free of charge only for noncommercial use (https://ambermd.org/GetAmber.php#amber). Single-point calculations at DFT and RI-MP2 levels were performed with ORCA 6.0, freely available for academic use only (https://www.faccts.de/orca/). Analysis of MD trajectories, metadynamics and machine-learning implementation were performed with PLUMED, open-source library released under GNU Lesser General Public License (https://www.plumed.org). The optimization of the HLDA variables from the descriptor distributions was performed with the python script deposited on the PLUMED-NEST repository (www.plumed-nest.org), with plumID:19.042. The python script used to reconstruct the high-level free energy surfaces with MetaFEP is deposited on the PLUMED-NEST repository (www.plumed-nest.org), with plumID:19.054. Topology and starting configuration files of PETase-PET4 and PETase-PEF4, MD simulation input files, external analysis and biasing PLUMED files, WTMD input files, MetaFEP input files (PBE, B3LYP, RI-MP2) and input/output files for the calculation of the condensed Fukui functions are publicly available on Zenodo at the following link: 10.5281/zenodo.14697147. Each additional file can be provided by the authors upon reasonable request.

Supporting Information

Local reactivity indexes of PEF4. The Supporting Information is available free of charge at https://pubs.acs.org/doi/10.1021/acscatal.5c01263.

Section S1: Details on the harmonic linear discriminant analysis procedure; Section S2: Details on the calculation of the perturbative term for the MetaFEP procedure; Section S3: Description of the global and local reactivity indices from conceptual DFT; Figure S1: Representation of the descriptors selected to optimize the reaction coordinate via HLDA; Figure S2: Distributions of the chemical descriptors extracted from standard QM/MM MD simulations; Figure S3: Descriptors of the interactions between the carbonyl group of the substrate and the oxyanion hole and conformation of the W185 side chain; Figure S4: Convergence of the MetaFEP corrections; Figure S5: Validation of the QM region with MetaFEP; Figure S6: Committor probability test for the validation of the transition states; Figure S7: Local philicity indexes of the PET4 and PEF4 ester groups far from the PETase binding site; Table S1: Descriptors selected for the optimization of the collective variable via HLDA; Table S2: PET4 and PEF4 interactions with the oxyanion hole at the stable states visited during the WTMD simulations; Table S3: Global reactivity indexes of PET4 and PEF4; Table S4: Local reactivity indexes of PET4; Table S5: Local reactivity indexes of PEF4 (PDF)

AUTHOR INFORMATION

Corresponding Authors

Alessandro Berselli − *Department of Chemical and Geological Sciences (DSCG), University of Modena and Reggio Emilia (UNIMORE), Modena 41125, Italy;* orcid.org/0000-0002-2241-3530; Email: alessandro.berselli@unimore.it

https://doi.org/10.1021/acscatal.5c01263
ACS Catal. 2025, 15, 10702−10721

GiovanniMaria Piccini − *Department of Chemical and Geological Sciences (DSCG), University of Modena and Reggio Emilia (UNIMORE), Modena 41125, Italy;* orcid.org/0000-0002-3511-4281; Email: giovannimaria.piccini@unimore.it

Authors

Maria Cristina Menziani − *Department of Chemical and Geological Sciences (DSCG), University of Modena and Reggio Emilia (UNIMORE), Modena 41125, Italy;* orcid.org/0000-0003-3428-5297

Francesco Muniz-Miranda − *Department of Chemical and Geological Sciences (DSCG), University of Modena and Reggio Emilia (UNIMORE), Modena 41125, Italy*

Complete contact information is available at: https://pubs.acs.org/10.1021/acscatal.5c01263

Author Contributions

A.B.: Data curation, Formal analysis, Conceptualization, Investigation, Visualization, Writing − original draft, Writing − review and editing. M.C. M.: Supervision, Writing − review and editing. G.P.: Formal analysis, Conceptualization, Supervision, Writing − review and editing. F.M.-M.: Project administration, Supervision, Writing − review and editing, Funding acquisition and resources.

Funding

The research was supported financially by the Italian "Ministero dell'Università e della Ricerca" (MUR) initiative PRIN 2022 on the project 2022W9XTYB entitled "Enzylearning" (020140_23_PRIN-2022 granted to FMM as "deputy PI") and the local "FAR2023-linea post-dottorato" initiative of UNIMORE.

Notes

In this work, no animal or human study is presented.
The authors declare no competing financial interest.

■ ACKNOWLEDGMENTS

We acknowledge CINECA awards under the ISCRA initiative (the Iscra C project HP10C1FZRH granted to AB and the Iscra C project HP10C4M2EF granted to FMM), for the availability of high-performance computing resources and support. We are also grateful to Prof. Dr. Alfonso Pedone for enabling us the access to the local computational cluster and Dr. Cristina Murari for the kind assistance. Finally, we thank Prof. Dr. Mirco Zerbetto (University of Padua, UNIPD, PI of the "Enzylearning" project) for the useful discussions.

■ REFERENCES

(1) Ali, S. S.; Elsamahy, T.; Koutra, E.; Kornaros, M.; El-Sheekh, M.; Abdelkarim, E. A.; Zhu, D.; Sun, J. Degradation of Conventional Plastic Wastes in the Environment: A Review on Current Status of Knowledge and Future Perspectives of Disposal. *Sci. Total Environ.* **2021**, *771*, 144719.

(2) Geyer, R.; Jambeck, J. R.; Law, K. L. Production, use, and fate of all plastics ever made. *Sci. Adv.* **2017**, *3* (7), No. e1700782.

(3) Berselli, A.; Ramos, M. J.; Menziani, M. C. Novel Pet-Degrading Enzymes: Structure-Function from a Computational Perspective. *ChemBiochem* **2021**, *22* (12), 2032−2050.

(4) Benyathiar, P.; Kumar, P.; Carpenter, G.; Brace, J.; Mishra, D. K. Polyethylene Terephthalate (PET) Bottle-to-Bottle Recycling for the Beverage Industry: A Review. *Polymers* **2022**, *14* (12), 2366.

(5) Petersen, F.; Hubbart, J. A. The Occurrence and Transport of Microplastics: The State of the Science. *Sci. Total Environ.* **2021**, *758*, 143936.

(6) Reichert, C. L.; Bugnicourt, E.; Coltelli, M.-B.; Cinelli, P.; Lazzeri, A.; Canesi, I.; Braca, F.; Martínez, B. M.; Alonso, R.; Agostinis, L.; Verstichel, S.; Six, L.; Mets, S. D.; Gómez, E. C.; Ißbrücker, C.; Geerinck, R.; Nettleton, D. F.; Campos, I.; Sauter, E.; Pieczyk, P.; Schmid, M. Bio-Based Packaging: Materials, Modifications, Industrial Applications and Sustainability. *Polymers* **2020**, *12* (7), 1558.

(7) Hiraga, K.; Taniguchi, I.; Yoshida, S.; Kimura, Y.; Oda, K. Biodegradation of Waste PET: A Sustainable Solution for Dealing with Plastic Pollution. *EMBO Rep.* **2019**, *20* (11), No. e49365.

(8) Eerhart, A. J. J. E.; Faaij, A. P. C.; Patel, M. K. Replacing Fossil Based PET with Biobased PEF; Process Analysis, Energy and GHG Balance. *Energy Environ. Sci.* **2012**, *5* (4), 6407−6422.

(9) Ganesh Kumar, A.; Anjana, K.; Hinduja, H.; K, K.; Dharani, G. Review on Plastic Wastes in Marine Environment - Biodegradation and Biotechnological Solutions. *Mar. Pollut. Bull.* **2020**, *150*, 110733.

(10) Almeida, E. L.; Carrillo Rincón, A. F.; Jackson, S. A.; Dobson, A. D. W. In Silico Screening and Heterologous Expression of a Polyethylene Terephthalate Hydrolase (PETase)-Like Enzyme (SM14est) With Polycaprolactone (PCL)-Degrading Activity, From the Marine Sponge-Derived Strain Streptomyces Sp. SM14. *Front. Microbiol.* **2019**, *10*, 2187.

(11) Wei, R.; Zimmermann, W. Biocatalysis as a Green Route for Recycling the Recalcitrant Plastic Polyethylene Terephthalate. *Microb. Biotechnol.* **2017**, *10* (6), 1302−1307.

(12) Yoshida, S.; Hiraga, K.; Takehana, T.; Taniguchi, I.; Yamaji, H.; Maeda, Y.; Toyohara, K.; Miyamoto, K.; Kimura, Y.; Oda, K. A Bacterium That Degrades and Assimilates Poly(Ethylene Terephthalate). *Science* **2016**, *351* (6278), 1196−1199.

(13) Austin, H. P.; Allen, M. D.; Donohoe, B. S.; Rorrer, N. A.; Kearns, F. L.; Silveira, R. L.; Pollard, B. C.; Dominick, G.; Duman, R.; Omari, K. E.; Mykhaylyk, V.; Wagner, A.; Michener, W. E.; Amore, A.; Skaf, M. S.; Crowley, M. F.; Thorne, A. W.; Johnson, C. W.; Woodcock, H. L.; McGeehan, J. E.; Beckham, G. T. Characterization and Engineering of a Plastic-Degrading Aromatic Polyesterase. *Proc. Natl. Acad. Sci. U. S. A.* **2018**, *115* (19), No. E4350−E4357.

(14) Heinks, T.; Hofmann, K.; Zimmermann, L.; Gamm, I.; Lieb, A.; Blach, L.; Wei, R.; Bornscheuer, T.; Thiele, U.; Hamel, J.; Langermann, J. V. Analysis of the Product-Spectrum during the Biocatalytic Hydrolysis of PEF (Poly(Ethylene Furanoate)) with Various Esterases. *RSC Sustain.* **2025**, *3* (3), 1346−1355.

(15) Fecker, T.; Galaz-Davison, P.; Engelberger, F.; Narui, Y.; Sotomayor, M.; Parra, L. P.; Ramírez-Sarmiento, C. A. Active Site Flexibility as a Hallmark for Efficient PET Degradation by I. Sakaiensis PETase. *Biophys. J.* **2018**, *114* (6), 1302−1312.

(16) Joo, S.; Cho, I. J.; Seo, H.; Son, H. F.; Sagong, H.-Y.; Shin, T. J.; Choi, S. Y.; Lee, S. Y.; Kim, K.-J. Structural Insight into Molecular Mechanism of Poly(Ethylene Terephthalate) Degradation. *Nat. Commun.* **2018**, *9*, 382.

(17) Han, X.; Liu, W.; Huang, J.-W.; Ma, J.; Zheng, Y.; Ko, T.-P.; Xu, L.; Cheng, Y.-S.; Chen, C.-C.; Guo, R.-T. Structural Insight into Catalytic Mechanism of PET Hydrolase. *Nat. Commun.* **2017**, *8* (1), 1−6.

(18) Kawai, F.; Iizuka, R.; Kawabata, T. Engineered Polyethylene Terephthalate Hydrolases: Perspectives and Limits. *Appl. Microbiol. Biotechnol.* **2024**, *108* (1), 404.

(19) de Castro, A. M.; Carniel, A.; Nicomedes Junior, J.; da Conceição Gomes, A.; Valoni, É. Screening of Commercial Enzymes for Poly(Ethylene Terephthalate) (PET) Hydrolysis and Synergy Studies on Different Substrate Sources. *J. Ind. Microbiol. Biotechnol.* **2017**, *44* (6), 835−844.

(20) Lu, H.; Diaz, D. J.; Czarnecki, N. J.; Zhu, C.; Kim, W.; Shroff, R.; Acosta, D. J.; Alexander, B. R.; Cole, H. O.; Zhang, Y.; Lynd, N. A.; Ellington, A. D.; Alper, H. S. Machine Learning-Aided Engineering of Hydrolases for PET Depolymerization. *Nature* **2022**, *604* (7907), 662−667.

(21) Sun, J.; Cui, Y.; Wu, B. GRAPE, a Greedy Accumulated Strategy for Computational Protein Engineering. *Methods Enzymol.* **2021**, *648*, 207−230.

(22) Cui, Y.; Chen, Y.; Liu, X.; Dong, S.; Tian, Y.; Qiao, Y.; Mitra, R.; Han, J.; Li, C.; Han, X.; Liu, W.; Chen, Q.; Wei, W.; Wang, X.; Du, W.; Tang, S.; Xiang, H.; Liu, H.; Liang, Y.; Houk, K. N.; Wu, B. Computational Redesign of a PETase for Plastic Biodegradation under Ambient Condition by the GRAPE Strategy. *ACS Catal.* **2021**, *11* (3), 1340−1350.
(23) Son, H. F.; Cho, I. J.; Joo, S.; Seo, H.; Sagong, H.-Y.; Choi, S. Y.; Lee, S. Y.; Kim, K.-J. Rational Protein Engineering of Thermo-Stable PETase from Ideonella Sakaiensis for Highly Efficient PET Degradation. *ACS Catal.* **2019**, *9* (4), 3519−3526.
(24) Arnal, G.; Anglade, J.; Gavalda, S.; Tournier, V.; Chabot, N.; Bornscheuer, U. T.; Weber, G.; Marty, A. Assessment of Four Engineered PET Degrading Enzymes Considering Large-Scale Industrial Applications. *ACS Catal.* **2023**, *13* (20), 13156−13166.
(25) Bell, E. L.; Smithson, R.; Kilbride, S.; Foster, J.; Hardy, F. J.; Ramachandran, S.; Tedstone, A. A.; Haigh, S. J.; Garforth, A. A.; Day, P. J. R.; Levy, C.; Shaver, M. P.; Green, A. P. Directed Evolution of an Efficient and Thermostable PET Depolymerase. *Nat. Catal.* **2022**, *5* (8), 673−681.
(26) Cui, Y.; Chen, Y.; Sun, J.; Zhu, T.; Pang, H.; Li, C.; Geng, W.-C.; Wu, B. Computational Redesign of a Hydrolase for Nearly Complete PET Depolymerization at Industrially Relevant High-Solids Loading. *Nat. Commun.* **2024**, *15* (1), 1417.
(27) Berselli, A.; Menziani, M. C.; Muniz-Miranda, F. Structure and Energetics of PET-Hydrolyzing Enzyme Complexes: A Systematic Comparison from Molecular Dynamics Simulations. *J. Chem. Inf. Model.* **2024**, *64* (21), 8236−8257.
(28) Jerves, C.; Neves, R. P. P.; Ramos, M. J.; da Silva, S.; Fernandes, P. A. Reaction Mechanism of the PET Degrading Enzyme PETase Studied with DFT/MM Molecular Dynamics Simulations. *ACS Catal.* **2021**, *11* (18), 11626−11638.
(29) Boneta, S.; Arafet, K.; Moliner, V. QM/MM Study of the Enzymatic Biodegradation Mechanism of Polyethylene Terephthalate. *J. Chem. Inf. Model.* **2021**, *61* (6), 3041−3051.
(30) Burgin, T.; Pollard, B. C.; Knott, B. C.; Mayes, H. B.; Crowley, M. F.; McGeehan, J. E.; Beckham, G. T.; Woodcock, H. L. The Reaction Mechanism of the Ideonella Sakaiensis PETase Enzyme. *Commun. Chem.* **2024**, *7* (1), 1−14.
(31) dos Santos, A. M.; da Costa, C. H. S.; Silva, P. H. A.; Skaf, M. S.; Lameira, J. Exploring the Reaction Mechanism of Polyethylene Terephthalate Biodegradation through QM/MM Approach. *J. Phys. Chem. B* **2024**, *128* (31), 7486−7499.
(32) García-Meseguer, R.; Ortí, E.; Tuñón, I.; Ruiz-Pernía, J. J.; Aragó, J. Insights into the Enhancement of the Poly(Ethylene Terephthalate) Degradation by FAST-PETase from Computational Modeling. *J. Am. Chem. Soc.* **2023**, *145* (35), 19243−19255.
(33) Feng, S.; Yue, Y.; Zheng, M.; Li, Y.; Zhang, Q.; Wang, W. IsPETase- and IsMHETase-Catalyzed Cascade Degradation Mechanism toward Polyethylene Terephthalate. *ACS Sustainable Chem. Eng.* **2021**, *9* (29), 9823−9832.
(34) Bolhuis, P. G.; Chandler, D.; Dellago, C.; Geissler, P. L. Transition Path Sampling: Throwing Ropes over Rough Mountain Passes, in the Dark. *Annu. Rev. Phys. Chem.* **2002**, *53*, 291−318.
(35) Peters, B.; Beckham, G. T.; Trout, B. L. Extensions to the Likelihood Maximization Approach for Finding Reaction Coordinates. *J. Chem. Phys.* **2007**, *127* (3), 034109.
(36) Piccini, G.; Mendels, D.; Parrinello, M. Metadynamics with Discriminants: A Tool for Understanding Chemistry. *J. Chem. Theory Comput.* **2018**, *14* (10), 5040−5044.
(37) Mendels, D.; Piccini, G.; Parrinello, M. Collective Variables from Local Fluctuations. *J. Phys. Chem. Lett.* **2018**, *9* (11), 2776−2781.
(38) Barducci, A.; Bussi, G.; Parrinello, M. Well-Tempered Metadynamics: A Smoothly Converging and Tunable Free-Energy Method. *Phys. Rev. Lett.* **2008**, *100* (2), 020603.
(39) Gaus, M.; Cui, Q.; Elstner, M. DFTB3: Extension of the Self-Consistent-Charge Density-Functional Tight-Binding Method (SCC-DFTB). *J. Chem. Theory Comput.* **2011**, *7* (4), 931−948.
(40) Koskinen, P.; Mäkinen, V. Density-Functional Tight-Binding for Beginners. *Comput. Mater. Sci.* **2009**, *47* (1), 237−253.
(41) Lee, K. H.; Schnupf, U.; Sumpter, B. G.; Irle, S. Performance of Density-Functional Tight-Binding in Comparison to Ab Initio and First-Principles Methods for Isomer Geometries and Energies of Glucose Epimers in Vacuo and Solution. *ACS Omega* **2018**, *3* (12), 16899.
(42) Zwanzig, R. W. High-Temperature Equation of State by a Perturbation Method. I. Nonpolar Gases. *J. Chem. Phys.* **1954**, *22* (8), 1420−1426.
(43) Piccini, G.; Parrinello, M. Accurate Quantum Chemical Free Energies at Affordable Cost. *J. Phys. Chem. Lett.* **2019**, *10* (13), 3727−3731.
(44) Geerlings, P.; De Proft, F.; Langenaeker, W. Conceptual Density Functional Theory. *Chem. Rev.* **2003**, *103* (5), 1793−1874.
(45) Choi, Y. K.; Park, S.-J.; Park, S.; Kim, S.; Kern, N. R.; Lee, J.; Im, W. CHARMM-GUI Polymer Builder for Modeling and Simulation of Synthetic Polymers. *J. Chem. Theory Comput.* **2021**, *17* (4), 2431−2443.
(46) Olsson, M. H. M.; Søndergaard, C. R.; Rostkowski, M.; Jensen, J. H. PROPKA3: Consistent Treatment of Internal and Surface Residues in Empirical pKa Predictions. *J. Chem. Theory Comput.* **2011**, *7* (2), 525−537.
(47) Søndergaard, C. R.; Olsson, M. H. M.; Rostkowski, M.; Jensen, J. H. Improved Treatment of Ligands and Coupling Effects in Empirical Calculation and Rationalization of pKa Values. *J. Chem. Theory Comput.* **2011**, *7* (7), 2284−2295.
(48) da Costa, C. H. S.; dos Santos, A. M.; Alves, C. N.; Martí, S.; Moliner, V.; Santana, K.; Lameira, J. Assessment of the PETase Conformational Changes Induced by Poly(Ethylene Terephthalate) Binding. *Proteins: struct., Funct., Bioinf.* **2021**, *89* (10), 1340−1352.
(49) Wei, R.; Song, C.; Gräsing, D.; Schneider, T.; Bielytskyi, P.; Böttcher, D.; Matysik, J.; Bornscheuer, U. T.; Zimmermann, W. Conformational Fitting of a Flexible Oligomeric Substrate Does Not Explain the Enzymatic PET Degradation. *Nat. Commun.* **2019**, *10*, 5581.
(50) Phillips, J. C.; Hardy, D. J.; Maia, J. D. C.; Stone, J. E.; Ribeiro, J. V.; Bernardi, R. C.; Buch, R.; Fiorin, G.; Hénin, J.; Jiang, W.; McGreevy, R.; Melo, M. C. R.; Radak, B. K.; Skeel, R. D.; Singharoy, A.; Wang, Y.; Roux, B.; Aksimentiev, A.; Luthey-Schulten, Z.; Kalé, L. V.; Schulten, K.; Chipot, C.; Tajkhorshid, E. Scalable Molecular Dynamics on CPU and GPU Architectures with NAMD. *J. Chem. Phys.* **2020**, *153* (4), 044130.
(51) Case, D. A.; Aktulga, H. M.; Belfon, K.; Ben-Shalom, I. Y.; Berryman, J. T.; Brozell, S. R.; Cerutti, D. S.; Cheatham, T. E., III; Cisneros, G. A.; Cruzeiro, V. W. D.; *Amber 2022*, University of California; San Francisco, 2022.
(52) Case, D. A.; Aktulga, H. M.; Belfon, K.; Cerutti, D. S.; Cisneros, G. A.; Cruzeiro, V. W. D.; Forouzesh, N.; Giese, T. J.; Götz, A. W.; Gohlke, H.; Izadi, S.; Kasavajhala, K.; Kaymak, M. C.; King, E.; Kurtzman, T.; Lee, T.-S.; Li, P.; Liu, J.; Luchko, T.; Luo, R.; Manathunga, M.; Machado, M. R.; Nguyen, H. M.; O'Hearn, K. A.; Onufriev, A. V.; Pan, F.; Pantano, S.; Qi, R.; Rahnamoun, A.; Risheh, A.; Schott-Verdugo, S.; Shajan, A.; Swails, J.; Wang, J.; Wei, H.; Wu, X.; Wu, Y.; Zhang, S.; Zhao, S.; Zhu, Q.; Cheatham, T. E. I.; Roe, D. R.; Roitberg, A.; Simmerling, C.; York, D. M.; Nagan, M. C.; Merz, K. M., Jr AmberTools. *J. Chem. Inf. Model.* **2023**, *63* (20), 6183−6191.
(53) Neese, F. The ORCA Program System. *Wiley Interdiscip. Rev.: Comput. Mol. Sci.* **2012**, *2* (1), 73−78.
(54) Maier, J. A.; Martinez, C.; Kasavajhala, K.; Wickstrom, L.; Hauser, K. E.; Simmerling, C. ff14SB: Improving the Accuracy of Protein Side Chain and Backbone Parameters from ff99SB. *J. Chem. Theory Comput.* **2015**, *11* (8), 3696−3713.
(55) Jorgensen, W. L.; Chandrasekhar, J.; Madura, J. D.; Impey, R. W.; Klein, M. L. Comparison of Simple Potential Functions for Simulating Liquid Water. *J. Chem. Phys.* **1983**, *79*, 926−935.
(56) Darden, T.; York, D.; Pedersen, L. Particle Mesh Ewald: An N·log(N) Method for Ewald Sums in Large Systems. *J. Chem. Phys.* **1993**, *98* (12), 10089−10092.

https://doi.org/10.1021/acscatal.5c01263
ACS Catal. 2025, 15, 10702−10721

(57) Berendsen, H. J. C.; Postma, J. P. M.; van Gunsteren, W. F.; DiNola, A.; Haak, J. R. Molecular Dynamics with Coupling to an External Bath. *J. Chem. Phys.* **1984**, *81* (8), 3684−3690.
(58) Bonomi, M.; Branduardi, D.; Bussi, G.; Camilloni, C.; Provasi, D.; Raiteri, P.; Donadio, D.; Marinelli, F.; Pietrucci, F.; Broglia, R. A.; Parrinello, M. PLUMED: A Portable Plugin for Free-Energy Calculations with Molecular Dynamics. *Comput. Phys. Commun.* **2009**, *180* (10), 1961−1972.
(59) Ryckaert, J.-P.; Ciccotti, G.; Berendsen, H. J. C. Numerical Integration of the Cartesian Equations of Motion of a System with Constraints: Molecular Dynamics of n-Alkanes. *J. Comput. Phys.* **1977**, *23* (3), 327−341.
(60) Miyamoto, S.; Kollman, P. A. SETTLE: An Analytical Version of the SHAKE and RATTLE Algorithm for Rigid Water Models. *J. Comput. Chem.* **1992**, *13* (8), 952−962.
(61) Laio, A.; Parrinello, M. Escaping Free-Energy Minima. *Proc. Natl. Acad. Sci. U. S. A.* **2002**, *99* (20), 12562−12566.
(62) Huber, T.; Torda, A. E.; van Gunsteren, W. F. Local Elevation: A Method for Improving the Searching Properties of Molecular Dynamics Simulation. *J. computer-Aided Mol. Des.* **1994**, *8* (6), 695−708.
(63) Perdew, J. P.; Burke, K.; Ernzerhof, M. Generalized Gradient Approximation Made Simple. *Phys. Rev. Lett.* **1996**, *77* (18), 3865−3868.
(64) Ditchfield, R.; Hehre, W. J.; Pople, J. A. Self-Consistent Molecular-Orbital Methods. An Extended Gaussian-Type Basis for Molecular-Orbital Studies of Organic Molecules. *J. Chem. Phys.* **1971**, *54* (2), 724−728.
(65) Becke, A. D. Density-functional thermochemistry. III. The role of exact exchange. *J. Chem. Phys.* **1993**, *98* (7), 5648−5652.
(66) Weigend, F.; Ahlrichs, R. Balanced Basis Sets of Split Valence, Triple Zeta Valence and Quadruple Zeta Valence Quality for H to Rn: Design and Assessment of Accuracy. *Phys. Chem. Chem. Phys.* **2005**, *7* (18), 3297−3305.
(67) Møller, C.; Plesset, M. S. Note on an Approximation Treatment for Many-Electron Systems. *Phys. Rev.* **1934**, *46* (7), 618.
(68) Feyereisen, M.; Fitzgerald, G.; Komornicki, A. Use of Approximate Integrals in Ab Initio Theory. An Application in MP2 Energy Calculations. *Chem. Phys. Lett.* **1993**, *208* (5), 359−363.
(69) Dunning, T. H., Jr Gaussian Basis Sets for Use in Correlated Molecular Calculations. I. The Atoms Boron through Neon and Hydrogen. *J. Chem. Phys.* **1989**, *90* (2), 1007−1023.
(70) Weigend, F. Accurate Coulomb-Fitting Basis Sets for H to Rn. *Phys. Chem. Chem. Phys.* **2006**, *8* (9), 1057−1065.
(71) Weigend, F. Hartree−Fock Exchange Fitting Basis Sets for H to Rn. *J. Comput. Chem.* **2008**, *29* (2), 167−175.
(72) Domingo, L. R.; Ríos-Gutiérrez, M.; Pérez, P. Applications of the Conceptual Density Functional Theory Indices to Organic Chemistry Reactivity. *Molecules* **2016**, *21* (6), 748.
(73) Parr, R. G.; Yang, W. Density Functional Approach to the Frontier-Electron Theory of Chemical Reactivity. *J. Am. Chem. Soc.* **1984**, *106* (14), 4049−4050.
(74) Parr, R. G.; Weitao, Y.; Parr, R. G.; Weitao, Y. Density-Functional Theory of Atoms and Molecules. In *International Series of Monographs on Chemistry*; Oxford University Press: Oxford, NY, 1995.
(75) Chattaraj, P. K.; Maiti, B.; Sarkar, U. Philicity: A Unified Treatment of Chemical Reactivity and Selectivity. *J. Phys. Chem. A* **2003**, *107* (25), 4973−4975.
(76) Legon, A. C. Prereactive Complexes of Dihalogens XY with Lewis Bases B in the Gas Phase: A Systematic Case for the Halogen Analogue B Small Middle Dot Small Middle Dot Small Middle dotXY of the Hydrogen Bond B Small Middle Dot Small Middle Dot Small Middle dotHX. *Angew. Chem., Int. Ed.* **1999**, *38* (18), 2686−2714.
(77) Yang, W.; Mortier, W. J. The Use of Global and Local Molecular Parameters for the Analysis of the Gas-Phase Basicity of Amines. *J. Am. Chem. Soc.* **1986**, *108* (19), 5708−5711.
(78) Parr, R. G.; Szentpály, L. V.; Liu, S. Electrophilicity Index. *J. Am. Chem. Soc.* **1999**, *121* (9), 1922−1924.
(79) Pratihar, S.; Roy, S. Nucleophilicity and Site Selectivity of Commonly Used Arenes and Heteroarenes. *J. Org. Chem.* **2010**, *75* (15), 4957−4963.
(80) Arulmozhiraja, S.; Kolandaivel, P. Condensed Fukui Function: Dependency on Atomic Charges. *Mol. Phys.* **1997**, *90* (1), 55−62.
(81) Langenaeker, W.; De Proft, F.; Geerlings, P. Electron Correlation Effects on Fukui Functions. *J. Mol. Struct.* **1996**, *362* (2), 175−179.
(82) De Proft, F.; Martin, J. M. L.; Geerlings, P. Calculation of Molecular Electrostatic Potentials and Fukui Functions Using Density Functional Methods. *Chem. Phys. Lett.* **1996**, *256* (4), 400−408.
(83) Contreras, R. R.; Fuentealba, P.; Galván, M.; Pérez, P. A Direct Evaluation of Regional Fukui Functions in Molecules. *Chem. Phys. Lett.* **1999**, *304* (5), 405−413.
(84) Thanikaivelan, P.; Padmanabhan, J.; Subramanian, V.; Ramasami, T. Chemical Reactivity and Selectivity Using Fukui Functions: Basis Set and Population Scheme Dependence in the Framework of B3LYP Theory. *Theor. Chem. Acc.* **2002**, *107* (6), 326−335.
(85) Mulliken, R. S. Electronic Population Analysis on LCAO−MO Molecular Wave Functions. I. *J. Chem. Phys.* **1955**, *23* (10), 1833−1840.
(86) Breneman, C. M.; Wiberg, K. B. Determining Atom-Centered Monopoles from Molecular Electrostatic Potentials. The Need for High Sampling Density in Formamide Conformational Analysis. *J. Comput. Chem.* **1990**, *11* (3), 361−373.
(87) Hirshfeld, F. L. Bonded-Atom Fragments for Describing Molecular Charge Densities. *Theoret. Chim. Acta* **1977**, *44* (2), 129−138.
(88) Verstraelen, T.; Vandenbrande, S.; Heidar-Zadeh, F.; Vanduyfhuys, L.; Van Speybroeck, V.; Waroquier, M.; Ayers, P. W. Minimal Basis Iterative Stockholder: Atoms in Molecules for Force-Field Development. *J. Chem. Theory Comput.* **2016**, *12* (8), 3894−3912.
(89) Peters, B. Using the Histogram Test to Quantify Reaction Coordinate Error. *J. Chem. Phys.* **2006**, *125* (24), 241101.
(90) Chattaraj, P. K.; Sarkar, U.; Roy, D. R. Electrophilicity Index. *Chem. Rev.* **2006**, *106* (6), 2065−2091.
(91) Erickson, E.; Shakespeare, T. J.; Bratti, F.; Buss, B. L.; Graham, R.; Hawkins, M. A.; König, G.; Michener, W. E.; Miscall, J.; Ramirez, K. J.; Rorrer, N. A.; Zahn, M.; Pickford, A. R.; McGeehan, J. E.; Beckham, G. T. Comparative Performance of PETase as a Function of Reaction Conditions, Substrate Properties, and Product Accumulation. *ChemSuschem* **2022**, *15* (1), No. e202101932.
(92) Eyring, H. The Activated Complex in Chemical Reactions. *J. Chem. Phys.* **1935**, *3* (2), 107−115.
(93) Chen, C.-C.; Han, X.; Li, X.; Jiang, P.; Niu, D.; Ma, L.; Liu, W.; Li, S.; Qu, Y.; Hu, H.; Min, J.; Yang, Y.; Zhang, L.; Zeng, W.; Huang, J.-W.; Dai, L.; Guo, R.-T. General Features to Enhance Enzymatic Activity of Poly(Ethylene Terephthalate) Hydrolysis. *Nat. Catal.* **2021**, *4* (5), 425−430.
(94) Jäckering, A.; van der Kamp, M.; Strodel, B.; Zinovjev, K. Influence of Wobbling Tryptophan and Mutations on PET Degradation Explored by QM/MM Free Energy Calculations. *J. Chem. Inf. Model.* **2024**, *64* (19), 7544−7554.
(95) Sun, L.; Wang, J.; Mahmud, S.; Jiang, Y.; Zhu, J.; Liu, X. New Insight into the Mechanism for the Excellent Gas Properties of Poly(Ethylene 2,5-Furandicarboxylate) (PEF): Role of Furan Ring's Polarity. *Eur. Polym. J.* **2019**, *118*, 642−650.
(96) Tournier, V.; Topham, C. M.; Gilles, A.; David, B.; Folgoas, C.; Moya-Leclair, E.; Kamionka, E.; Desrousseaux, M.-L.; Texier, H.; Gavalda, S.; Cot, M.; Guémard, E.; Dalibey, M.; Nomme, J.; Cioci, G.; Barbe, S.; Chateau, M.; André, I.; Duquesne, S.; Marty, A. An Engineered PET Depolymerase to Break down and Recycle Plastic Bottles. *Nature* **2020**, *580* (7802), 216−219.
(97) Kumar, V.; Pellis, A.; Wimmer, R.; Popok, V.; Christiansen, J. D. C.; Varrone, C. Efficient Depolymerization of Poly(Ethylene 2,5-Furanoate) Using Polyester Hydrolases. *ACS Sustainable Chem. Eng.* **2024**, *12* (26), 9658−9668.

https://doi.org/10.1021/acscatal.5c01263
ACS Catal. 2025, 15, 10702−10721

(98) Cribari, M. A.; Unger, M. J.; Unarta, I. C.; Ogorek, A. N.; Huang, X.; Martell, J. D. Ultrahigh-Throughput Directed Evolution of Polymer-Degrading Enzymes Using Yeast Display. *J. Am. Chem. Soc.* **2023**, *145* (50), 27380−27389.

https://doi.org/10.1021/acscatal.5c01263
ACS Catal. 2025, 15, 10702−10721